International Journal of Multiphase Flow 42 (2012) 80–95

Contents lists available at SciVerse ScienceDirect

International Journal of Multiphase Flow

journal homepage: www.elsevier.com/locate/ijmulflow

Turbulence modulation and microbubble dynamics in vertical channel flow

D. Molin [a], C. Marchioli [a,b], A. Soldati [a,b,*]

[a] Centro Interdipartimentale di Fluidodinamica e Idraulica, Università degli Studi di Udine, Udine, Italy
[b] Department of Fluid Mechanics, CISM, 33100 Udine, Italy

ARTICLE INFO

Article history:
Received 17 October 2011
Received in revised form 10 January 2012
Accepted 18 January 2012
Available online 8 February 2012

Keywords:
Microbubbles
Turbulence modulation
Direct numerical simulation
Lagrangian tracking
Two-way coupling
Lift force model

ABSTRACT

In this paper we examine the mutual interactions between microbubbles and turbulence in vertical channel flow. An Eulerian–Lagrangian approach based on pseudo-spectral direct numerical simulation is used: bubbles are momentum coupled with the fluid and are treated as pointwise spheres subject to gravity, drag, added mass, pressure gradient, Basset and lift forces. Two different flow configurations (upward and downward channel flow of water at shear Reynolds number $Re_\tau = 150$) and four different bubble diameters are considered, assuming that bubbles are non-deformable (i.e. small Eotvos number) and contaminated by surfactants (i.e. no-slip condition applies at bubble surface). Confirming previous knowledge, we find macroscopically different bubble distribution in the two flow configurations, with lift segregating bubbles at the wall in upflow and preventing bubbles from reaching the near-wall region in downflow. Due to local momentum exchange with the carrier fluid and to the differences in bubble distribution, we also observe significant increase (resp. decrease) of both wall shear and liquid flowrate in upflow (resp. downflow). We propose a novel force scaling to examine results in vertical turbulent bubbly flows, which can help to judge differences in the turbulence features due to bubble presence. By examining two-phase flow energy spectra, we show that bubbles determine an enhancement (resp. attenuation) of energy at small (resp. large) flow scales, a feature already observed in homogeneous isotropic turbulence. Bubble-induced flow field modifications, in turn, alter significantly the dynamics of the bubbles and lead to different trends in preferential concentration and wall deposition. In this picture, a crucial role is played by the lift force, which is a delicate issue when accurate models of shear flows with bubbles are sought. We analyze and discuss all the observed trends emphasizing the impact that the lift force model has on the simulations.

1. Introduction

Turbulent bubbly flows are commonly encountered in environmental processes and industrial applications. In natural flows bubbles are important in interfacial transport phenomena such as the uptake of greenhouse gases, e.g. methane and carbon dioxide, by the ocean (Thorpe, 1982), or the atmospheric exchange of oxygen with hypoxic rivers, lakes and oceans (Turney and Banerjee, 2008). The variety of instances is even wider in technology. Limiting the analysis to non-boiling gravity-driven flows, buoyant bubbles are commonly used to enhance turbulent mixing of dispersed reagents in devices such as bubble columns (Delnoij et al., 1999; Lain et al., 1999; Mudde, 2005; Mudde et al., 2009) and gas-lift reactors (Korpijarvi et al., 1999; Guet and Ooms, 2006). In all these situations, dispersion of bubbles occurs in a non-uniform fashion and gives raise to complex interactions with the turbulent flow structures. Experiments (Tomiyama et al., 2002; Hosokawa et al., 2010) and simulations (Ervin and Tryggvason, 1997; Lu and Tryggvason, 2006, 2007; Climent and Magnaudet, 2006) have shown that non-uniform distribution and bubbles–turbulence interplay, together with bubble size distribution, can affect significantly the overall evolution of the two-phase system by changing the flow hydrodynamics and altering the interfacial transfer rates. These phenomena, rich in physics and intrinsically complex, have strong modelling issues due to the multiscale nature of turbulent transfer phenomena (Mudde, 2005). Our study is motivated by the need to extend current physical understanding of microbubbles–turbulence interaction, still incomplete even in semi-dilute systems, and to establish a benchmark for further comparisons. In particular, we focus on pressure-driven liquid flows laden with gas microbubbles.

Current challenges in the analysis of pressure-driven bubbly flows deal with the high degree of unsteadiness and complexity manifested by liquid turbulence and bubble dispersion patterns. Several questions are still open and concern the modalities by which the carrier fluid determines bubble spatial distribution (and in turn bubble velocity distribution). In an effort to clarify these modalities, Giusti et al. (2005) used an Eulerian–Lagrangian approach based on Direct Numerical Simulation (DNS) to study the dispersion of small non-deformable bubbles in vertical channel

* Corresponding author. Tel.: +39 0432 558020; fax: +39 0432 558027.
E-mail address: soldati@uniud.it (A. Soldati).

0301-9322/$ - see front matter © 2012 Elsevier Ltd. All rights reserved.
doi:10.1016/j.ijmultiphaseflow.2012.01.010

flow assuming very dilute conditions (no feedback of bubbles on turbulence), a simple framework to investigate two-phase systems like bubble columns or gas-lift reactors which is also relevant to the small-scale dynamics of more general turbulent flows. The main finding of Giusti et al. (2005) is related to bubble behavior near the wall, where bubbles segregate preferentially in high-speed regions in the downflow case, whereas non-preferential distribution is observed in the upflow case.

In this paper, we build on the results of Giusti et al. (2005) extending the analysis to flows with larger gas fraction where the flow can be modified by bubbles via momentum exchange. We also consider bubble size effects, equally important in determining the overall behavior of the two-phase system. Finally, we adopt a more accurate lift force model which accounts for wall effects (Takemura and Magnaudet, 2003). Modifications on fluid velocity, bubble velocity and spatial bubble distribution are examined to characterize bubble preferential concentration and wall accumulation. These modifications are discussed in the limit of dilute bubble loading and negligible direct hydrodynamic interactions between bubbles. To our knowledge, there is no other numerical study that addresses these issues in bounded flows by taking into account collective bubble effects on turbulence. Many papers (e.g. Xu et al., 2002; Ferrante and Elghobashi, 2004; van den Berg et al., 2006; Jacob et al., 2010; Yeo et al., 2010) consider momentum coupling to evaluate drag reduction phenomena. Other analyses consider homogeneous isotropic turbulence (Ferrante and Elghobashi, 2003; van den Berg et al., 2006; Mazzitelli and Lohse, 2009; Yeo et al., 2010), spatially-developing turbulent boundary layers (Ferrante and Elghobashi, 2004; Climent and Magnaudet, 2006) or channel flow without gravity (Xu et al., 2002). Vertical channel/pipe flow simulations are available, yet only considering large, deformable bubbles (Lu and Tryggvason, 2006, 2007, 2008; Hosokawa and Tomiyama, 2010). Here, we focus rather on many small, non-deformable bubbles which can change, due to gravitational pull, the overall pressure drop of the system.

The paper is organized as follows. First, we summarize the basic features of the numerical method and the simulation parameters. Simulation parameters were chosen to mimic bubble columns or gas-lift reactors operating in the homogeneous (or dispersed) regime, which is found at relatively low superficial gas velocity, and is characterized by small, spherical or near-spherical bubbles (Lucas et al., 2005). The velocity fields of both fluid and bubbles are then analyzed to highlight modifications induced by collective effects in situations when direct hydrodynamic interactions between bubbles can be neglected. We follow by a discussion of preferential concentration and near-wall segregation, and conclude with a quantitative analysis of the two-phase flow energy spectra and of the forces acting on the bubbles to show the role played by the lift force, but also the importance of the model chosen to reproduce its effects in the equations of particle motion.

2. Physical problem and numerical methodology

The flow is driven by an imposed pressure gradient, with bubbles injected at void fraction low enough to ensure dilute system conditions and negligible bubble–bubble interactions. We consider air bubbles with density $\rho_p = 1.3\ \mathrm{kg\,m^{-3}}$ and diameters ranging from 110 to 330 μm (see Table 1); the carrier fluid is water, with density $\rho = 10^3\ \mathrm{kg\,m^{-3}}$ and kinematic viscosity $\nu = 10^{-6}\ \mathrm{m^2\,s^{-1}}$. The reference geometry is shown (with the coordinate system) in Fig. 1. In the numerical experiments referring to downward flow (DWF hereinafter), gravity is directed along the negative x-direction ($\mathbf{g} = -g\hat{\mathbf{e}}_x$), and along the positive x-direction ($\mathbf{g} = +g\hat{\mathbf{e}}_x$) in upward flow (UPF hereinafter). The flow field is periodic both in the streamwise and in the spanwise directions, and no-slip conditions are applied at the walls. The size of the computational domain is $L_x \times L_y \times L_z = 4\pi h \times 2\pi h \times 2h$, where h is the half wall-to-wall distance. The domain size was chosen to ensure that two-point correlations of the fluid velocity components reach a zero value ahead of the outlet section in each homogeneous direction.

Table 1
Parameters relative to the simulation of bubble dispersion. Superscript + identifies dimensionless variables. N_p is the number of tracked bubbles.

d_p (μm)	d_p^+	τ_p (μs)	τ_p^+	$\tilde{\tau}_p(ms)$	$\tilde{\tau}_p^+$	N_p
330	2.475	7.87	4.42×10^{-4}	3.033	1.71×10^{-1}	6,713
220	1.650	3.50	1.11×10^{-4}	1.348	7.58×10^{-2}	22,659
165	1.275	1.97	1.97×10^{-4}	0.758	4.26×10^{-2}	53,704
110	0.825	0.87	4.92×10^{-5}	0.337	1.89×10^{-2}	181,340

2.1. Equations for the fluid phase and flow solver

The governing equations for the fluid are continuity and Navier–Stokes equations, which in dimensionless form read as:

$$\frac{\partial u_i}{\partial x_i} = 0, \tag{1}$$

$$\frac{\partial u_i}{\partial t} + u_j \frac{\partial u_i}{\partial x_j} = -\frac{\partial p}{\partial x_i} + \delta_{1,i} + \frac{1}{Re_\tau}\frac{\partial^2 u_i}{\partial x_j \partial x_j} + f_{2W,i}, \tag{2}$$

where u_i is the ith component of the fluid velocity vector, p is the fluctuating kinematic pressure, $\delta_{1,i}$ is the mean pressure gradient that drives the flow, and $Re_\tau = h\,u_\tau/\nu$ is the shear Reynolds number based on the shear velocity:

$$u_\tau = \sqrt{\delta_{1,i}\frac{h}{\rho}}. \tag{3}$$

Note that, anticipating pressure drop changes due to bubbles, the shear velocity is not defined using the shear stress at the wall, τ_w, as usually done in single-phase problems. The last term on the right-hand side of Eq. (2), $f_{2W,i}$, represents the inter-phase momentum coupling, given by the force per unit volume exerted by the bubbles on the fluid, and is modelled using the well-known PSI-Cell (Particle-Source-In-Cell) method proposed by Crowe et al. (1977). This method does not include the effect of the particle wake, which becomes important for particle Reynolds numbers much higher than those obtained in our simulations (Yuu et al., 2002). Eqs. (1) and (2) were written neglecting effects due to local variations of the bubble volume fraction, Φ_V. According to Elghobashi (1994), this approach is valid for $\Phi_V < 10^{-3}$: higher values of the volume fraction, which may occur due to preferential concentration effects, would inevitably affect the accuracy of the approach and limit the applicability of its predictions (Ferrante and Elghobashi, 2004).

Eqs. (1) and (2) were solved directly using a pseudo-spectral method, which transforms the field variables into wavenumber space to discretize the governing equations. All quantities are expressed by Fourier expansions in the homogeneous directions x and y, and by Chebyshev polynomials in the wall-normal direction z (details in Soldati and Banerjee, 1998). All simulations were run at $Re_\tau = 150$. This value corresponds to a shear velocity equal to $7.5 \times 10^{-3}\ \mathrm{m\,s^{-1}}$ in a channel with $h = 0.02$ m. Calculations are done using variables in wall units, made dimensionless using u_τ, ν and ρ, and identified with the superscript +. The non-dimensional size of the computational domain is then $L_x^+ \times L_y^+ \times L_z^+ = 1885 \times 942 \times 300$. The domain is discretized by $N_x \times N_y \times N_z = 128 \times 128 \times 129$ grid points, uniformly distributed in the streamwise and spanwise directions to provide spacings equal to $\delta x^+ \approx 14.72$ and $\delta y^+ \approx 7.36$ in wall units. In the wall-normal direction, grid points

are clustered in the near-wall region. The distance between two neighboring points ranges from $\delta z^+_{min} = 0.045$ at the walls to $\delta z^+_{max} = 3.682$ in the center of the channel. The grid resolution is thus sufficient to describe the smallest length scale in the flow: the non-dimensional Kolmogorov length scale, η^+_K, varies along the wall-normal direction from a minimum value $\eta^+_K = 1.6$ at the wall to a maximum value $\eta^+_K = 3.6$ at the centerline (Marchioli et al., 2006). The step size for time integration was chosen based on the response time of the tracked bubbles (see next paragraph) with the minimum value $\delta t^+ = 0.0095$ for the 110 μm bubbles and the maximum value $\delta t^+ = 0.036$ for the 330 μm bubbles.

2.2. Equations for the dispersed phase and Lagrangian bubble tracking

Bubbles obey the following Lagrangian equation of motion in vector form:

$$\frac{d\mathbf{v}_p}{dt} = \underbrace{\left(1-\frac{\rho}{\rho_p}\right)\mathbf{g}}_{Gravity} + \underbrace{\frac{(\mathbf{u}_{@p}-\mathbf{v}_p)}{\tau_p}C_{SN}C_W}_{Drag} + \underbrace{\frac{\rho}{\rho_p}\frac{D\mathbf{u}_{@p}}{Dt}}_{Pressure\ Grad.} + \underbrace{C_L\frac{\rho}{\rho_p}\left[(\mathbf{u}_{@p}-\mathbf{v}_p)\times\boldsymbol{\omega}_{@p}\right]+f_{LW}\hat{\mathbf{e}}_z}_{Lift} + \underbrace{\frac{9\mu}{d_p\rho_p\sqrt{\pi\nu}}\int_0^t\left(\frac{d\mathbf{u}_{@p}}{dt}-\frac{d\mathbf{v}_p}{dt}\right)\frac{d\tau}{(t-\tau)^{0.5}}}_{Basset} + \underbrace{\frac{\rho}{2\rho_p}\left(\frac{D\mathbf{u}_{@p}}{Dt}-\frac{d\mathbf{v}_p}{dt}\right)}_{Added\ Mass}, \tag{4}$$

where bold-faced letters are vectors; $\mathbf{v}_p$ is bubble instantaneous velocity; $\mathbf{u}_{@p}$ and $\boldsymbol{\omega}_{@p}$ are fluid velocity and vorticity at bubble location; $\mathbf{g}$ is gravitational acceleration; and τ_p is the bubble response time:

$$\tau_p = \frac{\rho_p d_p^2}{18\mu}, \tag{5}$$

with d_p the bubble diameter, and μ the fluid dynamic viscosity. Eq. (5) can be corrected to account for added mass effects, thus obtaining $\tilde{\tau}_p = \tau_p[1+\rho/(2\rho_p)] \simeq 385.6\tau_p$. Dimensional and non-dimensional values of d_p, τ_p and $\tilde{\tau}_p$ are given in Table 1; and yield large near-wall values of the *bubblance* parameter defined as (Lance and Bataille, 1991):

$$b = \frac{1}{2}\frac{\Phi_V v_T^2}{\langle u'^2\rangle}, \tag{6}$$

with $\Phi_V v_T^2$ the kinetic energy due to bubble motion ($v_T = g\tilde{\tau}_p$ being the bubble rise velocity in still fluid) and $\langle u'^2\rangle$ the kinetic energy of the fluid velocity fluctuations before bubble injection. In our problem, bubbles in the wall proximity are in the $b \simeq \mathcal{O}(1)$ regime and are expected to modify turbulence significantly. We also remark that, even if bubble size is varied over a rather large range of diameters, no locking of bubbles into near-wall fluid velocity streaks is observed. This unphysical effect appears when the domain extent in the streamwise direction is not long enough to apply periodic boundary conditions properly.

To analyze the effect that microbubbles can produce collectively on the two-phase system, the flow should be driven by $\mathcal{O}(10^4)$ bubbles at least. Due to current computational capabilities, it is not feasible to track these many bubbles using fully-resolved simulations, which can treat up to $\mathcal{O}(10^2)$ bubbles (Esmaeeli and Tryggvason, 2005). Following Climent and Magnaudet (1999, 2006) and Mazzitelli and Lohse (2009), we adopted an alternative Eulerian–Lagrangian approach that allows to track large swarms of bubbles at reduced computational costs by (i) modeling bubbles as points, (ii) neglecting near-field interactions among bubbles, and (iii) using effective force models for drag and lift. The point-bubble model, in particular, is a key feature in view of the range of bubble diameters we had to select to emphasize lift effects. The downsize of this choice is that, for the problem under investigation (gas–liquid flow), these effects are maximized for bubble diameters that become larger than the wall-normal grid spacing within few viscous units from the wall. Here, the pointwise approach shows intrinsic limitations in terms of accuracy that at present can not be removed. In the downflow case, bubbles are kept away from the near-wall region by lift (Giusti et al., 2005) so inaccuracies due to bubble-to-gridsize ratios larger than unity are expected to be negligible. In the upflow case, bubbles accumulate well inside the viscous sublayer and our results can be considered reliable only when the center of the bubble is at least one diameter away from the wall (for the larger 330 μm bubbles, this corresponds to a minimum bubble-to-wall distance of about three wall units). A detailed investigation of bubble behavior very near the wall, however, would require an accurate modelling of bubble–bubble interaction in area densely populated by bubbles, which is beyond the scope of this paper. In our opinion, this "range of validity" is sufficient to describe segregation patterns and accumulation fluxes since all bubble–turbulence interactions relevant to these phenomena occur outside the viscous sublayer. We stress here that, for the parameter range of this work, other modelling approaches would be hardly viable with present-day methods and computers.

The time derivative $D\mathbf{u}_{@p}/Dt = \partial\mathbf{u}_{@p}/\partial t + \mathbf{u}_{@p}\cdot\nabla\mathbf{u}_{@p}$ is the total acceleration of the fluid at bubble location, whereas $d\mathbf{u}_{@p}/dt = \partial\mathbf{u}_{@p}/\partial t + \mathbf{v}_p\cdot\nabla\mathbf{u}_{@p}$ is calculated along bubble trajectory. Finally, the coefficients C_{SN}, C_W and C_L represent corrections to drag and lift, respectively. The coefficient $C_{SN} = 1 + 0.15Re_p^{0.687}$ provides a non-linear correction to the Stokesian drag force when the bubble Reynolds number, $Re_p = |\mathbf{u}_{@p} - \mathbf{v}_p|d_p/\nu$ becomes larger than unity (Schiller and Naumann, 1933). In our simulations, the mean value of the bubble Reynolds number, $\overline{Re}_p$, changes significantly with the bubble diameter but not much with the flow configuration: both in upflow and in downflow, we find $\overline{Re}_p \simeq 0.75,\ 1.9,\ 4$ and 11.2 for the 110, 165, 220, and 330 μm bubbles, respectively. The standard deviation from such mean values varies between 0.18 and 0.34 depending on bubble size, and corresponds to corrections of Stokes drag below 10% for the smaller bubbles and up to 80% for the larger bubbles. The coefficient C_W accounts for further modifications to the drag force due to the presence of a solid boundary in the vicinity of the bubble. Following Fukagata et al. (2001), the equations used to calculate C_W, in directions parallel ($_\parallel$) and orthogonal ($_\perp$) to the wall, are:

$$C_{W_\parallel} = \left[1-\frac{9}{16}\left(\frac{d^+}{2z^+}\right)+\frac{1}{8}\left(\frac{d^+}{2z^+}\right)^3-\frac{45}{256}\left(\frac{d^+}{2z^+}\right)^4-\frac{1}{16}\left(\frac{d^+}{2z^+}\right)^5\right]^{-1}$$
$$C_{W_\perp} = \left[\left\{1-\frac{9}{8}\left(\frac{d^+}{2z^+}\right)+\frac{1}{2}\left(\frac{d^+}{2z^+}\right)^2\right\}\cdot\left\{1-exp\left(-2.686\left(\frac{2z^+}{d^+}-0.999\right)\right)\right\}\right]^{-1} \tag{7}$$

where the term $d^+/2z^+$ indicates the ratio between bubble radius and the distance between wall and bubble center. The coefficient C_L in the lift force term accounts for corrections due to small/large bubble Reynolds number. We calculated C_L as:

$$C_L = \begin{cases} C_{L_{McL}} = \left[5.816\left(\frac{Sr_p}{2Re_p}\right)^{0.5} - 0.875\frac{Sr_p}{2}\right]\frac{3}{4Sr_p}\frac{J(\epsilon)}{2.255} & \text{for } Re_p < 1 \\ C_{L_{McL}}\frac{5-Re_p}{4} + C_{L_{KK}}\frac{Re_p-1}{4} & \text{for } 1 < Re_p < 5 \\ C_{L_{KK}} = \left[K_0\left(\frac{Sr_p}{2}\right)^{0.9} + K_1\left(\frac{Sr_p}{2}\right)^{1.1}\right]\frac{3}{4Sr_p} & \text{for } Re_p > 5 \end{cases} \tag{8}$$

In Eq. (8) $C_{L_{McL}}$ represents the coefficient calculated following McLaughlin (1991). The function $J(\epsilon)$ is reported in McLaughlin (1991), with $\epsilon = (Sr_p/Re_p)^{0.5}$ and $Sr_p = |(\mathbf{u}_{@p} - \mathbf{v}_p)\times\boldsymbol{\omega}_{@p}|d_p/|\mathbf{u}_{@p} - \mathbf{v}_p|^2$. The coefficient $C_{L_{KK}}$ is calculated as in Kurose and Komori (1999), where K_0 and K_1 are tabulated as functions of Re_p. Based on the values of Re_p in our simulations, we note that $C_L = C_{L_{McL}}$ for the 110 μm bubbles only, while $C_L = C_{L_{KK}}$ for the 330 μm bubbles. For the intermediate-size bubbles (165 and 220 μm), in most of the occurrencies Re_p is in such range that the lift coefficient is computed as linear interpolation between $C_{L_{McL}}$ and $C_{L_{KK}}$.

Aerodynamic lift is computed accounting also for the term f_{LW}, the wall-induced extra lift acting on each bubble. This term was not considered in Giusti et al. (2005), and is computed here according to Takemura and Magnaudet (2003):

$$f_{LW} = \frac{3}{4}\frac{\rho}{\rho_p d_p} V_{LW}^2 C_{LW}, \tag{9}$$

where V_{LW} is the relative velocity between bubble and fluid in the wall-parallel (x,y)-plane, i.e. $V_{LW} = \{[(u_x)_{@p} - v_{p,x}]^2 + [(u_y)_{@p} - v_{p,y}]^2\}^{0.5}$, and C_{LW} is a non-dimensional coefficient computed as:

$$C_{LW} = C_{LW_0}\left(1 + 0.6Re_{LW}^{0.5} - 0.55Re_{LW}^{0.08}\right)^2 \cdot \left(\frac{1}{3}\frac{2z^+}{d_p^+}\right)^{-2\tanh(0.01Re_{LW})} \tag{10}$$

where $Re_{LW} = V_{LW}d_p/\nu$ is bubble Reynolds number based on the relative velocity V_{LW}, and C_{LW_0} is a coefficient that depends on the non-dimensional distance from the wall, $z^* = zV_{LW}/\nu$, according to the following equations:

$$C_{LW_0}\begin{cases} = \left[\frac{9}{8} + 5.78\times10^{-6}(z^*)^{4.58}\right]\beta^2\exp(-0.292z^*) & \text{for } z^* < 10 \\ = 8.94\beta^2(z^*)^{-2.09} & \text{for } z^* > 10 \end{cases} \tag{11}$$

Note that $\beta = 1$ for the case of contaminated bubbles (Takemura and Magnaudet, 2003).

Eq. (4) is similar to the equation of motion for small rigid spheres (Gatignol, 1983; Maxey and Riley, 1983), written here neglecting the second order terms (related to $\nabla\mathbf{u}_{@p}$) due to the small size of the bubbles (Rizk and Elghobashi, 1985). The rigid sphere approach is valid until the condition $Eo < 0.2$ is satisfied, where $Eo = d_p^2|\rho_p - \rho|g/\sigma_s$ is the Eotvos (or Bond) number and σ_s is the surface tension at fluid/bubble interface. For this study, we assumed $\sigma_s = 0.0728$ N/m, corresponding to an air/water interface at 20 °C. The resulting values of the Eotvos number are $E_0 \simeq 1{,}44\times10^{-2}$ for the 330 μm bubbles and $E_0 \simeq 1{,}6\times10^{-3}$ for the 110 μm bubbles. In solving Eq. (4), we also assumed that water contains surfactants: Under this hypothesis, a no-slip condition can be applied at bubble interface (Ferrante and Elghobashi, 2004), and bubble internal circulation can be neglected.

The trajectory of individual bubbles is obtained upon time integration of Eq. (4) using a 4th-order Runge–Kutta scheme: bubbles start from an initial random distribution over the computational domain with initial velocity equal to the fluid velocity at bubble location. Fluid velocity interpolation is performed using 6th-order Lagrangian polynomials (near the wall, the interpolation scheme switches to one-sided). The time-step size for bubble tracking was chosen equal to that of the fluid and corresponds to roughly one fifth of the corrected response time $\tilde{\tau}_p$ for a given bubble set (see Table 1). According to the Nyquist theorem, this ensures a faithful reproduction of bubble transient behavior (Elghobashi and Truesdell, 1992). Bubble-wall interaction is modelled by rigid elastic rebound, and bubbles are re-injected into the domain when they cross periodic boundaries in streamwise or spanwise direction. This procedure also allows to keep the average volume fraction of the bubbles constant in time.

2.3. Summary of simulations

The database developed for this study comprises eight simulations with two-way coupling (four bubble diameters and two flow configurations), all performed imposing the same average void fraction, $\Phi_V = 10^{-4}$, corresponding to an average mass fraction $\Phi_M = 1.3\times10^{-7}$. A larger void fraction would change the regime from bubbles transported by the fluid to fluid driven by bubble swarms (Mudde, 2005). For each simulation, its one-way coupling counterpart is available. The total simulation time for each run was $T_{UPF} \simeq 108$ s for the upflow case (in wall units $T_{UPF}^+ = 6120$), and $T_{DWF} \simeq 95$ s for the downflow case (in wall units $T_{DWF}^+ = 5400$). These times are sufficient for a fluid particle moving at the average fluid velocity to sweep the entire streamwise length of the channel more than forty times. The total tracking time was $T_{tr,UPF}^+ = 2880$ for the upflow case, and $T_{tr,DWF}^+ = 2160$ for the downflow case. Finally, the time span considered for averaging the statistics was $T_{avg}^+ \simeq 1500$ for all cases. We remark that, upon bubble injection, the momentum coupling introduces a "numerical perturbation" in the system and alters the wall shear stress. Once this perturbation is damped, the system reaches a new steady state characterized by constant average wall shear stress, and statistics can be gathered. The time evolution of the wall shear stress observed in our simulations is analyzed in detail in Section 3.

3. Results

In this section, upflow and downflow statistics of the velocity field for both fluid and bubbles are presented. Before discussing the results, it is crucial to stress on the changes of the wall shear, which will show on the quantitative figures of all dimensionless quantities. We thus start from a simple one-dimensional model in which bubbles act on the fluid as an additional pressure gradient that can eventually modify the shear stress at the wall. Through this model we can link directly bubble feedback onto turbulence, and we can devise a theoretical tool to look at the results.

3.1. Rescaling wall shear stress to account for bubble-induced modifications

Consider the flow (no matter if laminar or turbulent) in a vertical channel of size $L_x \times L_y \times L_z$. Let the flow be driven by an external imposed pressure difference ΔP (including the hydrostatic pressure difference required to balance the gravity force acting on the fluid). At steady state, the force balance is:

$$\Delta P \cdot \mathcal{A} = \tau_W \cdot \mathcal{P}, \rightarrow \tau_W = \frac{\Delta P}{L_x}\frac{L_z}{2} \tag{12}$$

where $\mathcal{A} = L_y \times L_z$ is the cross-sectional area, τ_W is the mean shear stress at the wall, and $\mathcal{P} = 2\cdot(L_x \times L_y)$ is the wetted perimeter. Consider now the bubble-laden case, in which N_p spherical bubbles (of volume $\mathcal{V}_p = d_p^3\pi/6$) are injected into the flow. Bubble feedback on the fluid can be quantified by the body force term $\mathbf{F}_{2w} = N_p \cdot \mathbf{F}_{2w,p}$ where $\mathbf{F}_{2w,p}$ is the force imposed on the fluid by the pth bubble. In the streamwise (vertical) direction, bubbles dynamics is mostly influenced by drag, gravity and buoyancy. Hence:

$$\mathbf{F}_{2w,p} = -\mathbf{F}_{drag} = \mathbf{F}_{buoy+grav} = (\rho - \rho_p)\mathcal{V}_p\mathbf{g}. \tag{13}$$

If it is further assumed that bubbles remain uniformly distributed in the channel then the total force $\mathbf{F}_{2w}$ is also uniformly distributed, and the effect of bubbles on the flow may be expressed in the form of an equivalent pressure difference imposed at the channel streamwise ends. In scalar form:

$$\Delta P_{eq,2w} = \frac{F_{2w}L_x}{\mathcal{V}} = N_p(\rho - \rho_p)\mathcal{V}_p g\frac{L_x}{\mathcal{V}} = \Phi_V(\rho - \rho_p)gL_x, \tag{14}$$

Table 2
Effect of bubbles on wall shear stress, shear velocity and shear Reynolds number. Values for bubble-laden flow with one-way coupling or unladen flow (first column) are compared against values for bubble-laden flow with two-way coupling (second column: upflow, third column: downflow). Definitions are as follows: $u_{\tau,2w,UPF}=\sqrt{\frac{\tau_{W,2w,UPF}}{\rho}}$, $u_{\tau,2w,DWF}=\sqrt{\frac{\tau_{W,2w,DWF}}{\rho}}$, $Re_{\tau,2w,UPF}=\frac{u_{\tau,2w,UPF}\cdot h}{\nu}$ and $Re_{\tau,2w,DWF}=\frac{u_{\tau,2w,DWF}\cdot h}{\nu}$.

Unladen flow	Bubble-laden flow (2-way)	
	Upflow (UPF)	Downflow (DWF)
$\tau_W^+=1$	$\tau_{W,2w,UPF}^+=1.3483$	$\tau_{W,2w,DWF}^+=0.6517$
$u_\tau=7.5$ mm s^{-1}	$u_{\tau,2w,UPF}=8.7$ mm s^{-1}	$u_{\tau,2w,DWF}=6.1$ mm s^{-1}
$Re_\tau=150$	$Re_{\tau,2w,UPF}=174.2$	$Re_{\tau,2w,DWF}=121.1$

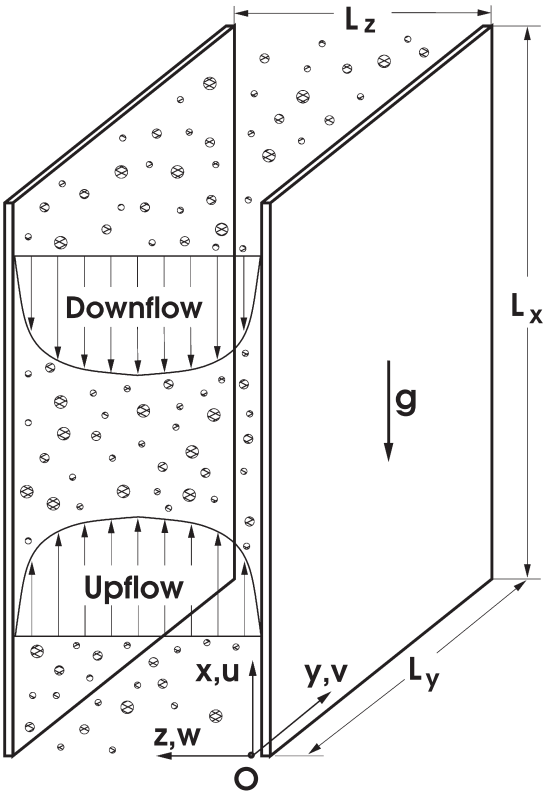

Fig. 1. Sketch of the computational domain.

where $\mathcal{V}$ is the volume occupied by the fluid in the channel, and $\Phi_V=N_p\mathcal{V}_p/\mathcal{V}$ is the void fraction. The wall shear stress with two-way coupling at steady state then becomes:

$$\tau_{W,2w}=\frac{\Delta P\pm\Delta P_{eq,2w}}{L_x}\frac{L_z}{2}=\left[\frac{\Delta P}{L_x}\pm\Phi_V(\rho-\rho_p)g\right]\frac{L_z}{2},$$

where sign + (resp. −) holds for the upflow (resp. downflow) case. In our channel $L_z=2h$, and we find: $\tau_{W,2w}=\tau_W\pm\Phi_V g(\rho-\rho_p)h$. In wall units, obtained normalizing by ρu_τ^2:

$$\tau_{W,2w}^+=1\pm\alpha g^+(1-\rho_p/\rho)Re_\tau. \tag{15}$$

Values of $\tau_{W,2w}$ obtained in our two-way coupled simulations are shown in Table 2. Due to the additional pressure difference induced by the bubbles, the wall shear stress in upflow ($\tau_{W,2w,UPF}^+$) increases with respect to the single-phase simulation, whereas the wall shear stress in downflow ($\tau_{W,2w,DWF}^+$) decreases. Changes of the wall shear stress correspond to changes of the shear velocity and, in turn, of the shear Reynolds number. Elaborating, in upflow (resp. downflow) the effect of bubbles on the fluid at $Re_\tau=150$ is equivalent to increasing (resp. decreasing) the shear Reynolds number to $Re_\tau,2w,UPF=174.2$ (resp. $Re_{\tau,2w,DWF}=121.1$) in a single-phase simulation. In the following paragraph, we will verify the validity of this prediction examining bubble-induced flowrate modifications.

3.2. Fluid velocity statistics

Fig. 2 shows the time evolution of $\tau_{W,2w}^+$. For ease of discussion, profiles in this figure, and in figures hereinafter unless otherwise stated, are relative to the 220 μm bubbles (solid lines), for which direct comparison against the results of Giusti et al. (2005) is available, and to the 110 μm bubbles (dashed lines), which will be used to highlight modifications due to bubble size. Results for the other two bubble sets ($d_p=165$ μm and $d_p=330$ μm) are qualitatively similar and will not be shown. The time span covered in this figure starts at $t^+=1800$ after inclusion of two-way coupling in the simulations (note that all statistics shown in this paper were gathered from this time instant onwards), and finishes at $t^+=3280$, when $\tau_{W,2w}^+$ has reached its steady-state value. In the downflow case, this value tends asymptotically to the theoretical prediction $\tau_{W,2w,DWF}^+=0.6517$ for both bubble sizes. This means that, at steady state, momentum transfer between fluid and bubbles reduces $\tau_{W,2w}^+$ with respect to unladen flow (dot-dashed line). In the upflow case,

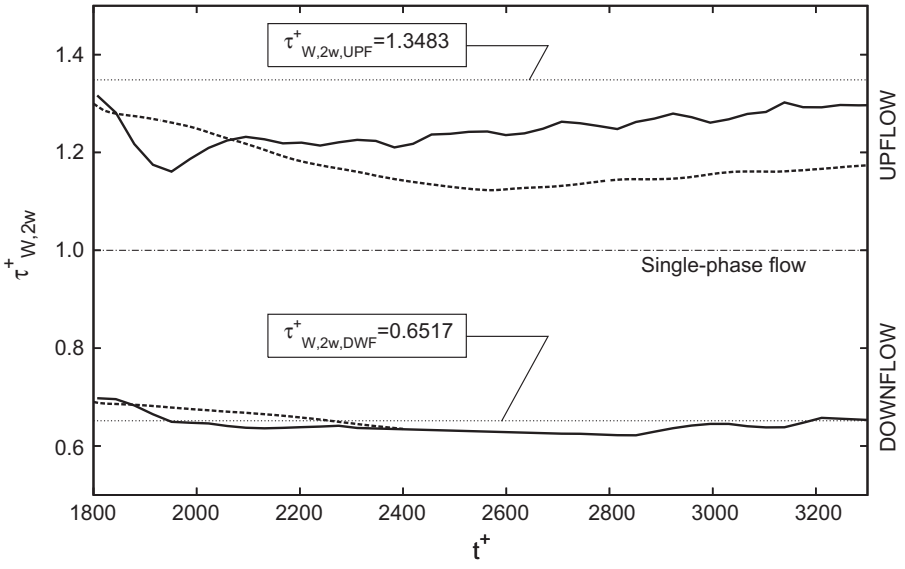

Fig. 2. Time evolution of wall shear stress, $\tau_{W,2w}^+$. Top-half panel: upflow simulations with two-way coupling; bottom-half panel: downflow simulations with two-way coupling. Lines are as follows: (- - -) 110 μm bubbles; (—) 220 μm bubbles; (-·-) unladen flow; (···) estimated value for $\tau_{W,2w}^+$ in two-way coupling simulations.

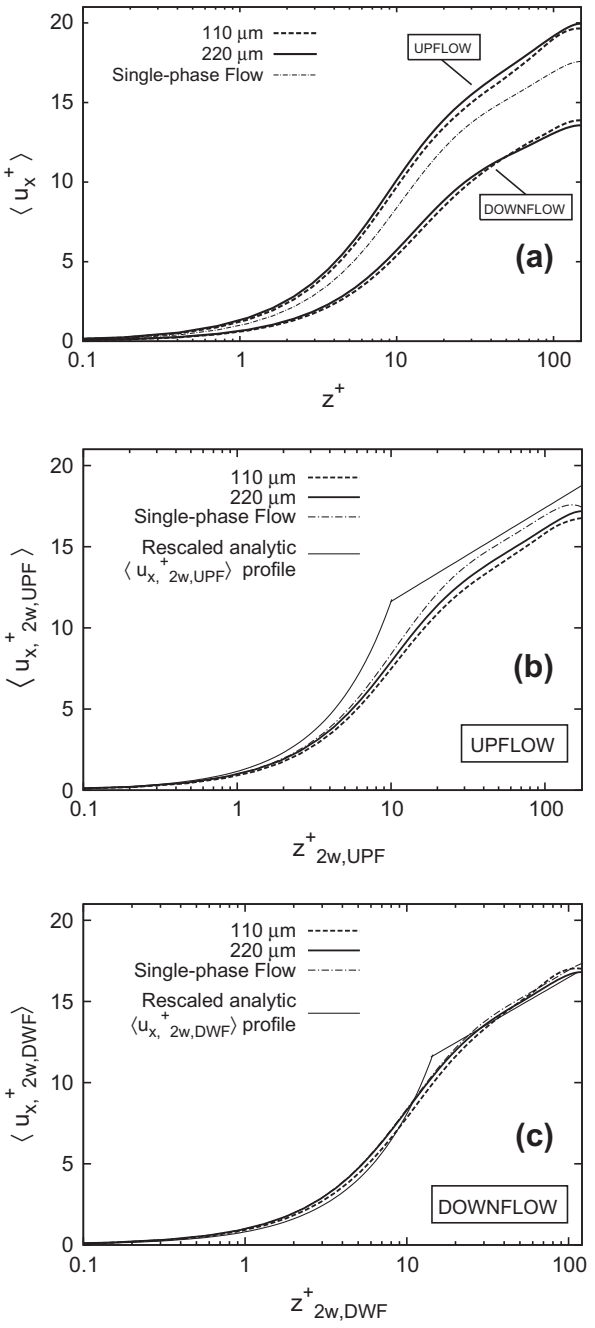

Fig. 3. Mean streamwise fluid velocity in two-way coupled simulations. Profiles in panels (b and c) are rescaled based on $u_{\tau,2w,UPF}$ for upflow and on $u_{\tau,2w,DWF}$ for downflow, respectively. Lines are as follows: (- - -) 110 μm bubbles; (—) 220 μm bubbles; (-·-) unladen flow.

values of $\tau^+_{W,2w}$ at steady-state are always smaller than the prediction $\tau^+_{W,2w,UPF} = 1.3483$, even though differences are larger for smaller bubbles. Bubble effects on wall shear stress correspond to variations of the streamwise fluid velocity profiles, which are shown in Fig. 3: Profiles for upflow/downflow laden with bubbles of diameter 110 μm and 220 μm are shown in Fig. 3a. Compared to unladen flow (dot-dashed line), the presence of bubbles increases the velocity in upflow (solid line), and decreases the velocity in downflow (dashed line). Profiles relative to bubbles with diameter 165 μm and 330 μm follow the same trend. This result is expected since bubbles rising in a co-current flow favor the upward transport of fluid, whereas bubbles rising in a counter-current flow hinder downward transport of fluid. To characterize bubble-induced effects in terms of equivalent pressure gradient, we renormalized the profiles shown in Fig. 3a replacing u_τ with $u_{\tau,2w,UPF}$ and $u_{\tau,2w,DWF}$ for upflow and downflow, respectively. Rescaled profiles are shown in Fig. 3b and in Fig. 3c, with thick lines referring to two-way coupled bubble-laden flow and thin lines referring to single-phase/one-way coupled flow. Analytic profiles and the wall-normal coordinate z^+ are also rescaled based on the proper value of the shear velocity. Fig. 3b shows that the difference observed in Fig. 3a is significantly reduced: for both bubble sizes the rescaled velocity $\left\langle u^+_{x,2w,UPF} \right\rangle = \langle u_{x,2w,UPF} \rangle / u_{\tau,2w,UPF}$ falls just slightly below the analytic profile and the computed single-phase/one-way coupled flow profile. The same trend is observed in downflow (Fig. 3c), where all profiles collapse onto each other almost perfectly. The improved agreement obtained upon rescaling support the conclusion that rising bubbles act on the fluid as an "equivalent", albeit non uniform, pressure gradient. This pressure gradient may either accelerate (in upflow) or decelerate (in downflow) the fluid: in both cases, bubbles will alter not only mean quantities but also turbulence intensities. This is demonstrated in Fig. 4, where we show the Root Mean Square (RMS) of the fluid velocity fluctuations, rescaled according to Table 2. In each panel, results obtained from two-way coupled simulations (thick lines) are compared against the reference one-way coupled simulations (thin lines). For the 220 μm bubbles only, the non-rescaled fluid RMS components are also shown for comparison purposes. Some general observations can be drawn from Fig. 4. First, without rescaling bubbles appear to have a significant effect on the intensity of velocity fluctuations, which are increased in upflow and decreased in downflow. This result is consistent with the variation of the flowrate discussed in Fig. 3: when the flowrate (the bulk Reynolds number) increases, an increase of turbulence intensity is expected and viceversa. Second, rescaled turbulence intensities in two-way coupled simulations compare reasonably well with turbulence intensities in pure-fluid simulations, indicating that turbulence in momentum-coupled bubble-laden upflow (resp. downflow) is similar to an unladen flow at suitably-chosen higher (resp. lower) Reynolds number. There are important differences however. In upflow, the rescaled streamwise RMS component is always lower than in single-phase/one-way coupled flow; in downflow, this undershoot is observed consistently for all three RMS components. These latter findings show some agreement with the experimental observations of Serizawa et al. (2004), who reported pseudo-laminarization in vertical pipe flow in presence of bubbles arguing that bubbles may reduce the capability of near-wall vortices to mix high-speed and low-speed fluid and, in turn, to sustain turbulent fluctuations. Third, bubble size has marginal effect on the overall system behavior: RMS profiles for the 110 μm bubbles and for the 220 μm bubbles overlap almost perfectly, with a slight underestimation observed only for the wall-normal component in downflow (Fig. 4f).

3.3. Bubble statistics

In this section, we discuss concentration and velocity statistics to quantify the influence of momentum exchange between the two phases on preferential segregation and wall fluxes. Results are then explained by analysis of the fluid energy spectra and evaluation of the forces acting on bubbles, in particular lift.

3.3.1. Momentum coupling effects on preferential concentration and wall accumulation

Several DNS-based studies of heavy particle dispersion in channel flow (see Soldati and Marchioli, 2009; and references therein) have demonstrated the strong correlation existing among coherent wall structures and particle transport mechanisms. In Fig. 5 we provide a pictorial view of transport mechanisms for the case of

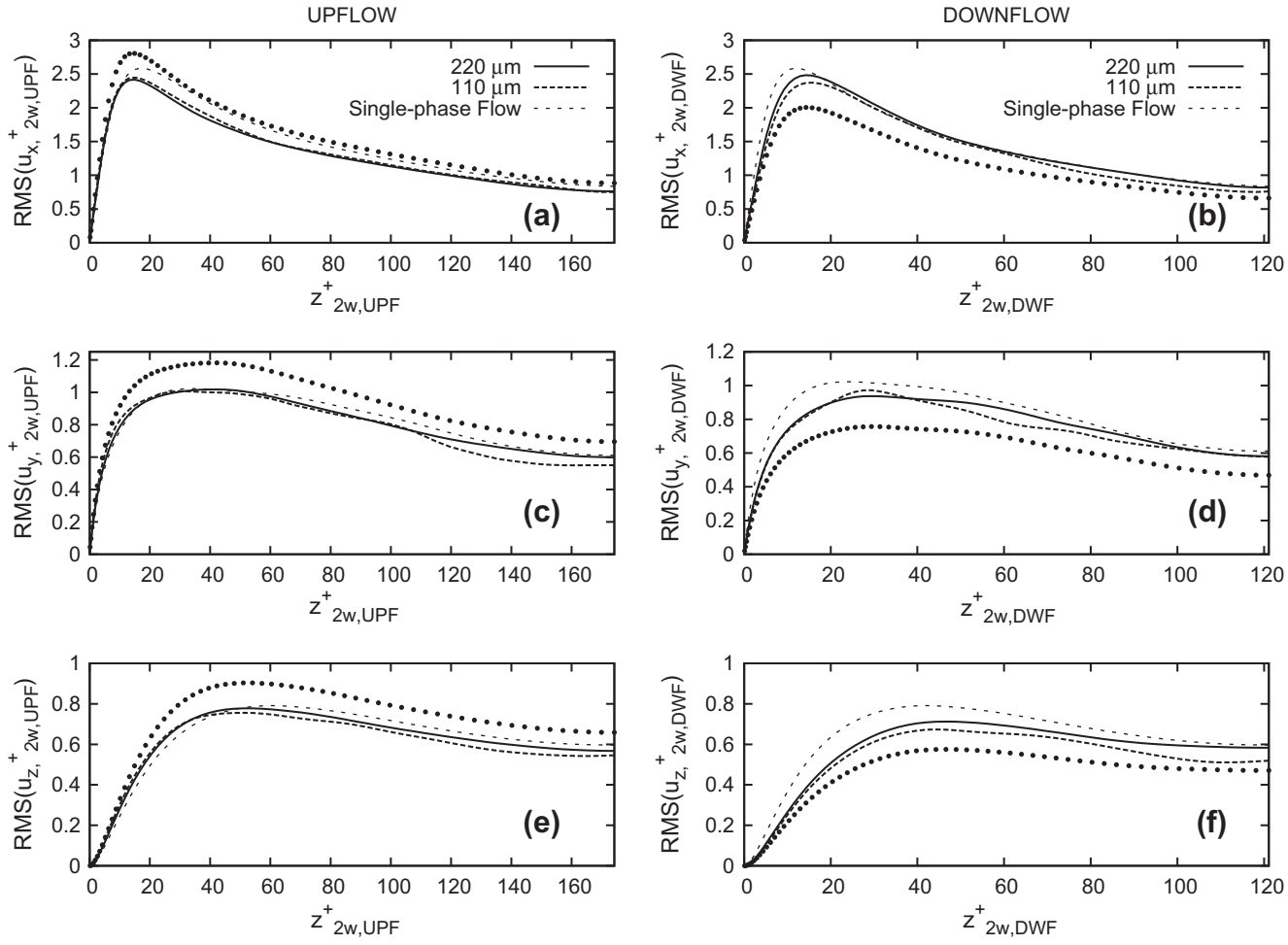

Fig. 4. Rescaled Root Mean Square (RMS) of fluid velocity in upflow [$RMS\left(u^{+}_{i,2w,UPF}\right) = RMS\left(u'_{i,2w,UPF}\right)/u_{\tau,2w,UPF}$; panels (a), (c) and (e)] and in downflow [$RMS(u^{+}_{i,2w,DWF}) = RMS\left(u'_{i,2w,DWF}\right)/u_{\tau,2w,DWF}$; panels (b), (d), and (f)]. Panels (a and b): streamwise RMS component; panels (c and d): spanwise RMS component; panels (e and f): wall-normal RMS component. Lines: (- - -) 110 μm bubbles; (—) 220 μm bubbles; (-·-) unladen flow. Symbols: (•) non-rescaled RMS components, $RMS\left(u^{+}_{i,2w,UPF}\right) = RMS\left(u'_{i,2w,UPF}\right)/u_{\tau}$ and $RMS\left(u^{+}_{i,2w,DWF}\right) = RMS\left(u'_{i,2w,DWF}\right)/u_{\tau}$, for two-way coupled simulations with the 220 μm bubbles.

microbubbles: one instantaneous snapshot of bubble spatial distribution in the near-wall region of the channel, focused on a cross-sectional window of the computational domain having streamwise thickness $\Delta x^{+} = 400$. All bubble classes are included in the snapshots, reproduced with diameters in the correct reciprocal dimensional scale. Notice that we can not scale bubble diameter to the box dimensions (the smallest bubbles would be invisible). The colored background represents the in-plane streamwise fluid velocity at $x^{+} = 800$, shown here to relate bubble distribution with the local flow structure. As already observed in many previous works (Serizawa et al., 1975; Hibiki et al., 2004; Giusti et al., 2005), bubbles in upflow (Fig. 5a) are transported towards the wall where they tend to accumulate regardless of their size; bubbles in downflow (Fig. 5b) are prevented from reaching the very near-wall region where practically no bubble is ever found. In both situations, bubbles maintain a rather uniform spatial distribution away from the wall and there is no clear evidence of segregation into clusters (van den Berg et al., 2006; Calzavarini et al., 2008).

In Fig. 6 we show the instantaneous concentration profiles in the wall-normal direction for the different bubble classes both in upflow (Fig. 6a) and downflow (Fig. 6b). Bubble concentration is computed at the final time step of the simulations: The flow domain was divided into $N_s = 193$ wall-parallel slabs of thickness $\Delta z^{+}(s) = \frac{Re_\tau}{\tanh(\gamma)}\left[\tanh\left(\gamma\frac{s}{N_s}\right) - \tanh\left(\gamma\frac{s-1}{N_s}\right)\right]$, where $s = 1,\ldots,N_s$ is the slab counter and $\gamma = 1.7$ is the stretching factor. The number of bubbles within each slab, $N_b(s,t)$, is counted and divided by the volume of that slab, V_s, to obtain local concentration $C = C(s,t) = N_b(s,t)/V_s$. Finally, C is normalized by its initial value, $C_0 = C(s,t=0)$. The ratio C/C_0 is bubble number density and will be larger than unity in the flow regions were bubbles tend to segregate and smaller than unity in the regions depleted of bubbles. Note that integration of C/C_0 over half cross section in the wall-normal direction gives a constant value equal to Re_τ in wall units. Fig. 6a shows that all bubble classes, with the exception of the 330 μm bubbles, undergo accumulation at the wall and a maximum is observed for the 165 μm bubbles (black circles). For the intermediate-size bubbles ($d_p = 110$, 165 and 220 μm) local variations of the volume fraction reach peak values of order 10^{-2}. These values are significantly larger than the threshold separating the dilute flow regime from the dense flow regime (Elghobashi, 1994), yet they are found only within a distance of one viscous unit from the wall. This distance corresponds to roughly one bubble diameter: our results, which apply to dilute flow conditions, may thus be considered reliable when bubbles are at least one diameter away from the wall.

Direct comparison of concentration profiles against Giusti et al. (2005) is only possible for the 220 μm bubbles (open squares). For these bubbles, inclusion of two-way coupling effects lowers the peak of concentration compared to one-way coupling results, making it quantitatively closer to experiments (see for instance Felton and Loth, 2001, 2002). A significant proportion of bubbles does not

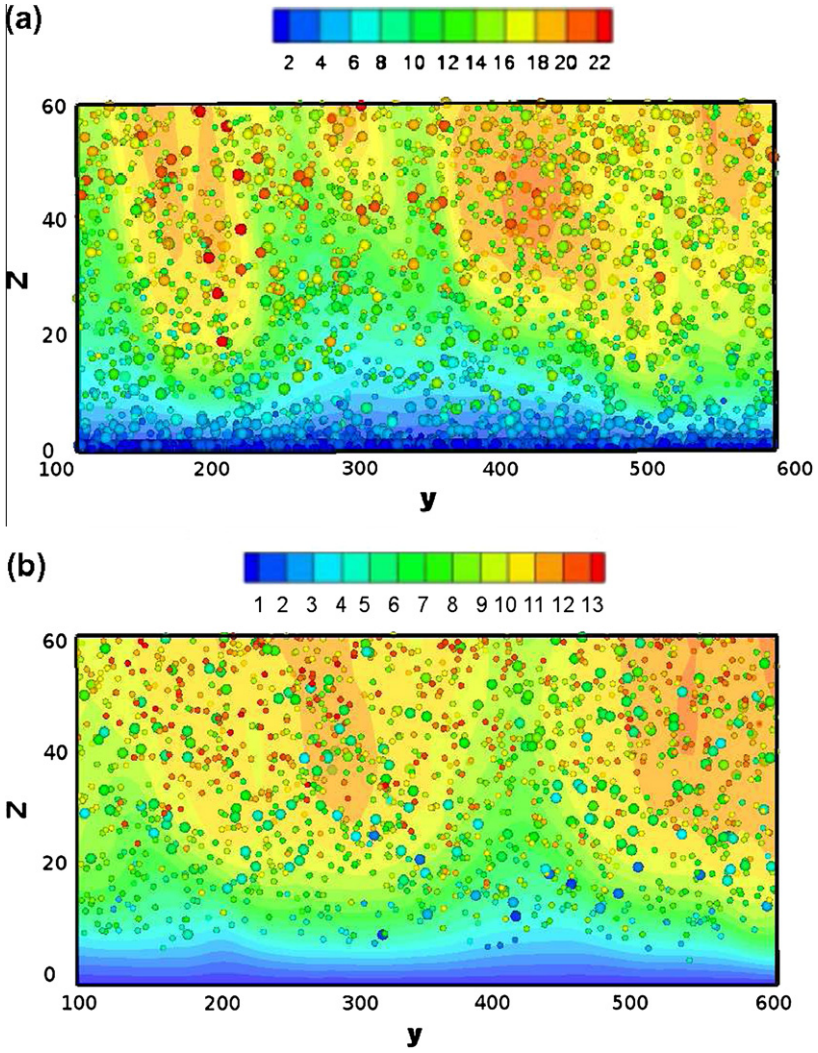

Fig. 5. Cross-sectional view of instantaneous bubbles distribution in the near wall region of the channel. A computational window in the range $600 < x^+ < 1000$, $100 < y^+ < 600$, $0 < z^+ < 60$ is considered. Bubbles are rendered as circles sized according to bubble diameter and colored according to bubble streamwise velocity. Bubbles are superposed to colormap of the instantaneous fluid streamwise velocity taken at $x^+ = 800$. Panels: (a) upflow; (b) downflow. (For color interpretation in this figure legend the reader is referred to see the web version of this article.)

migrate right at the wall anymore, leading to the formation of a bulge in the concentration profile ($1 < z^+ < 5$). No peak is observed for the 330 μm bubbles (black squares), which slowly move away from the viscous sublayer and migrate towards the center of the channel. To understand the change of shape in the concentration profile between the 220 μm bubbles and the 330μm bubbles, in Fig. 6a we included an additional class of bubbles with intermediate diameter ($d_p = 250$ μm, open triangles). It is apparent that, as bubble diameter increases, both regions of maximum peak and bulge are drained and the viscous sublayer becomes more and more depleted of bubbles. Bubbles concentration in downflow is shown in Fig. 6b: there is practically no bubble in the viscous sublayer, and bubble distribution away from the wall is nearly uniform. This behavior is in qualitative agreement with that observed in Giusti et al. (2005), the only two-way coupling effect being a sharper concentration gradient for $z^+ < 10$.

Bubble distribution in the wall region of the channel is related to bubble transfer fluxes in the wall-normal direction. Concentration build-up occurs in upflow because bubble transfer to the wall is more efficient than bubble transfer away from the wall during the time transient in which concentration is developing from the initial condition of random seeding: the resulting net flux of bubbles to the wall, k^+ in dimensionless units, is quantified in Table 3. We remark that this quantity is zero in downflow because transfer fluxes compensate each other and bubble concentration has already reached the steady state. To determine k^+ we computed the rate of change of the number $N(t)$ of bubbles with positive (resp. negative) wall-normal velocity which instantaneously cross an arbitrarily-chosen wall-parallel monitor surface in the near-wall region. A net mass flux of gas (bubbles), indicated here as J ($\mathrm{kg\,m^{-2}\,s^{-1}}$), is thus obtained and then normalized by the mean bulk concentration of bubbles, C_b ($\mathrm{kg\,m^{-1}}$), to get $k = J/C_b$. Given the number N_0 of tracked bubbles, J and C_b in non-dimensional form read as:

$$J^+(t^+) = \frac{1}{A^+}\cdot\frac{dN(t^+)}{dt^+}, C_b(t^+) = \frac{N_0 - N(t^+)}{V^+} \tag{16}$$

where $A^+ = L_x^+ L_y^+$ is the area of the monitor surface, $V^+ = A^+ z^+$ is the volume of fluid comprised between the monitor surface and the wall, and z^+ is the distance from the wall at which a bubble crosses the monitor surface, which we placed at $z^+ \simeq 2$, $z^+ \simeq 5$ and $z^+ \simeq 7$. Values of k^+ obtained for the 220 μm bubbles show that wallward mass fluxes are much less intense when bubbles can exchange momentum with the fluid, the reduction being of order 50% at all

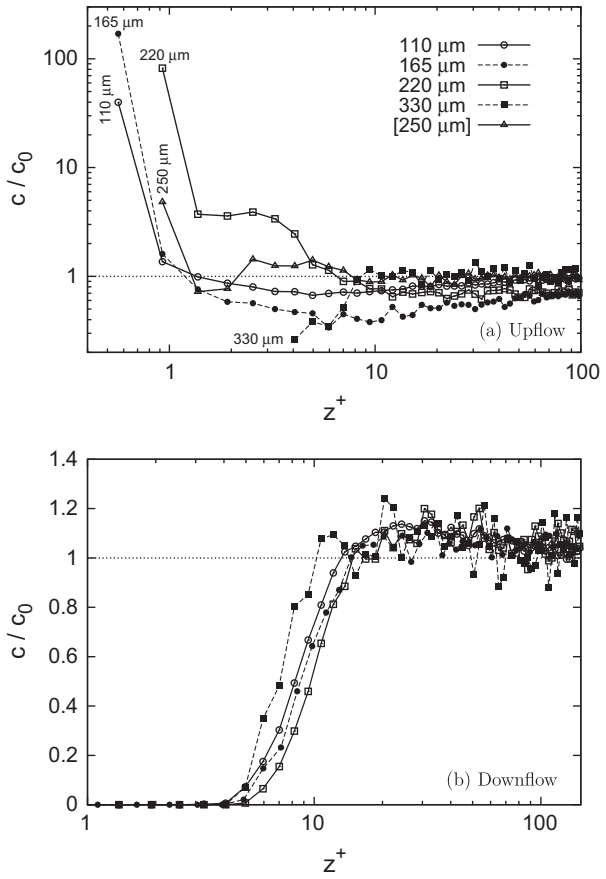

Fig. 6. Microbubble number density distribution in two-way coupled vertical channel flow. Panels: (a) upflow, (b) downflow. Symbols: (○) 110 μm bubbles, (●) 165 μm bubbles, (□) 220 μm bubbles, (■) 330 μm bubbles.

Table 3
Non-dimensional bubble wallward fluxes, k^+, as a function of bubble diameter, d_p, and location of the monitor surface from the wall, z^+, in upward channel flow.

Fluid-bubble coupling	Bubble diameter (d_p (μm))	Bubble wallward flux ($k^+ \times 10^{-5}$)		
		$z^+ \simeq 2$	$z^+ \simeq 5$	$z^+ \simeq 7$
One-way	220	0.29	0.59	0.81
	220	0.12	0.35	0.43
Two-way	165	0.46	1.11	1.61
	110	0.11	0.24	0.34

monitor surfaces. Considering values of k^+ obtained in two-way coupling simulations, it is confirmed that the 165 μm bubbles exhibit the strongest fluxes, in agreement with the results of Fig. 6.

3.3.2. Bubble velocity statistics

A statistical description of bubble velocity field and of the flow field seen by the bubbles can be useful to interpret the transport mechanisms discussed previously. In particular, time-averaged velocity statistics can be used to analyze the importance of bubbles–turbulence interactions on the two-phase system by correlating the turbulent field sampled by the bubbles with the mean turbulent field. In Figs. 7 and 8 we compare the mean streamwise velocity of the fluid, $\langle u_x^+ \rangle$, of the fluid seen by bubbles, $\langle u_x^+ \rangle_{@p}$ (evaluated upon interpolation of u_x^+ at the bubble location), and of the bubbles, $\langle v_{p,x}^+ \rangle$, for upflow and downflow respectively. Note that, since statistics in these figures are at steady state, the relative (slip) velocity between fluid and bubbles can be obtained directly as $\langle v_{slip,x}^+ \rangle = \langle (u_x^+)_{@p} - v_{p,x}^+ \rangle = \langle u_x^+ \rangle_{@p} - \langle v_{p,x}^+ \rangle$. In upflow (Fig. 7), there is no difference between the Eulerian flow field (solid line) and the flow field *seen* by the 110 μm (smaller) bubbles. A significant difference between the two fields is obtained for the larger bubbles in the region $2 < z^+ < 15$, where $\langle u_x^+ \rangle_{@p} < \langle u_x^+ \rangle$ and the concentration profile develops the bulge shown in Fig. 6. This behavior agrees with the observation that there is little or no bubble segregation in the core flow region and in the very-near wall region, but it may also indicate that large enough bubbles can produce strong turbulence modifications just across the viscous sublayer by collecting preferentially in low-speed zones. Examining the bubble velocity $\langle v_{p,x}^+ \rangle$, we find (as expected) that bubbles lead the fluid and the slip velocity deficit, nearly constant in the wall-normal direction, is that required for the drag force to counterbalance the buoyancy force in the streamwise direction. This deficit is larger for larger bubbles, but is reduced in the near-wall region due to the wall correction which increases the drag force.

In downflow (Fig. 8), we first observe that velocity profiles end at $z^+ \simeq 3$ for the 110 μm bubbles and at $z^+ \simeq 5$ for the 220 μm bubbles because no bubbles are found beyond these points. Second, the similarity between the fluid velocity profiles is lost when bubbles approach the wall: the fluid velocity seen becomes higher than the Eulerian velocity in the range $3 < z^+ < 15$ for the 110 μm bubbles, and (by larger amounts) in the range $5 < z^+ < 30$ for the 220 μm bubbles. Besides confirming that no preferential bubble distribution occurs in the center of the channel, this result also reveals that bubbles sample high-speed regions associated to coherent wallward fluxes of high-momentum fluid (sweep events). These events, however, are not able to carry the entrained bubbles

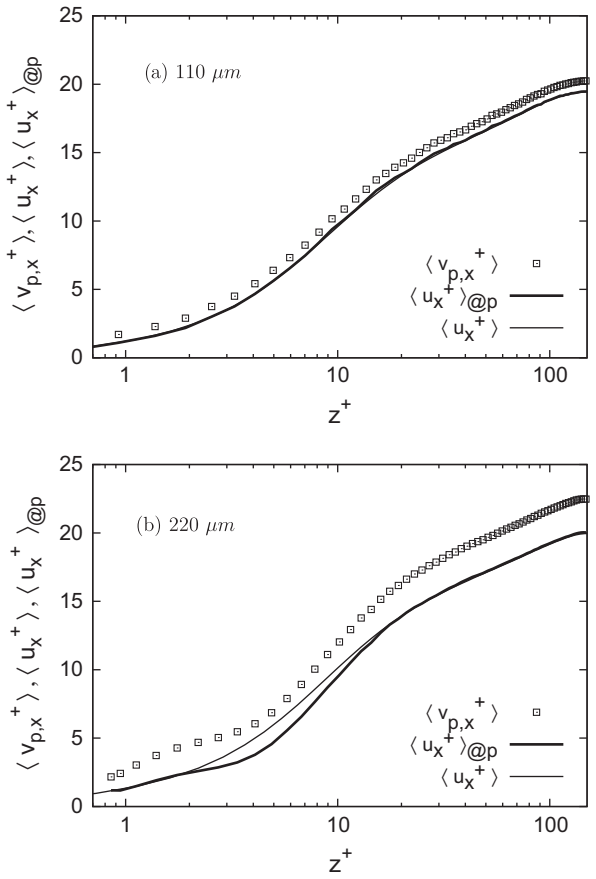

Fig. 7. Mean streamwise velocities in two-way coupled upflow: Panels: (a) 110 μm bubbles, (b) 220 μm bubbles. Lines and symbols: (□) bubble velocity, $\langle v_{p,x}^+ \rangle$; (—) Eulerian fluid velocity, $\langle u_x^+ \rangle$; (- - -) fluid velocity at bubble location, $\langle u_x^+ \rangle_{@p}$.

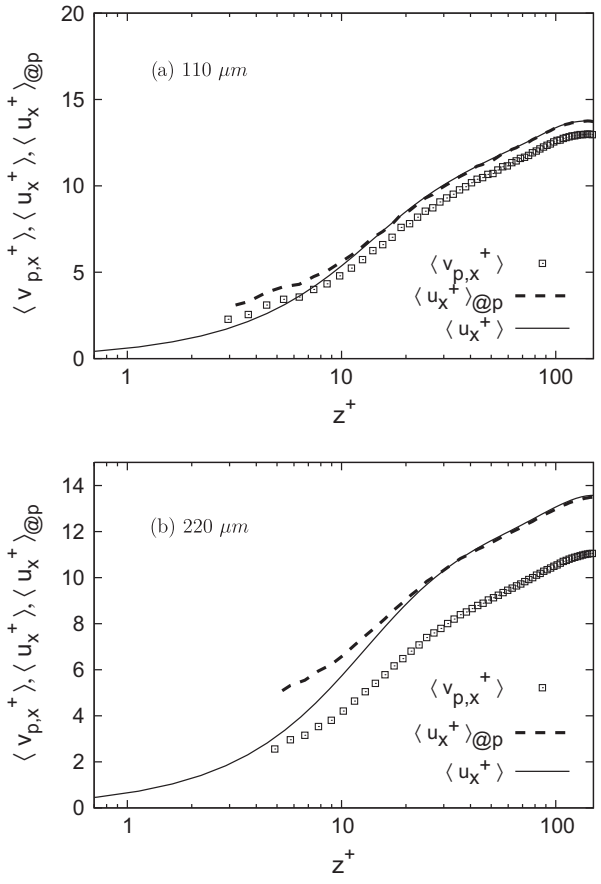

Fig. 8. Mean streamwise velocities in two-way coupled downflow: Panels: (a) 110 μm bubbles, (b) 220 μm bubbles. Lines and symbols: (□) bubble velocity, $\langle v_{p,x}^{+} \rangle$; (—) Eulerian fluid velocity, $\langle u_x^{+} \rangle$; (- - -) fluid velocity at bubble location, $\langle u_x^{+} \rangle_{@p}$.

right at the wall their action being contrasted by the lift force push, which becomes dominant in the vicinity of the wall (see Section 3.5). In this region, bubble preferential sampling is thus induced by lift rather than by inertia as it occurs for heavy particles. Finally, we observe that bubble velocity is always smaller than the fluid velocity seen and that this nearly-constant velocity gap increases with the size of bubbles so that larger bubbles lag the fluid everywhere. Present findings resemble those reported in Giusti et al. (2005) and indicate minor two-way coupling effects on the mean velocity fields.

Two-way coupling effects are more evident on turbulent fluctuations, as demonstrated by the higher-order velocity statistics. Here, we limit our analysis to the Root Mean Square (RMS) statistics, shown in Fig. 9 for upflow and in Fig. 10 for downflow. The RMS of bubble velocity fluctuations, $RMS(v'_{p,i})$ (open squares), is compared against the RMS of the Eulerian fluid velocity fluctuations, $RMS(u'_i)$ (solid line), and the RMS of the fluid velocity fluctuations *seen*, $RMS(u'_i)_{@p}$ (dashed line), for three different cases: two-way coupled simulations with 110 μm bubbles (left-hand column), two-way coupled simulations with 220 μm bubbles (middle column), and one-way coupled simulations with 220 μm bubbles (right-hand column). In two-way coupled upflow, the different RMS profiles do not change much with bubble diameter and overlap almost perfectly except in the streamwise direction (Fig. 9b). Due to bubble preferential distribution in low-speed regions (where turbulent fluctuations are lower), the streamwise velocity fluctuations of both bubbles and fluid seen are smaller than the Eulerian counterpart in the viscous sublayer, but reach a higher peak at $z^+ \simeq 10$. This behavior is observed also in one-way coupling simulations, yet it is enhanced by momentum exchange. In agreement with the observed increase of flowrate, the RMS values resulting from two-way coupling simulations are always higher than those obtained from one-way coupling simulations. Note that the bulge in the $RMS(v'_{p,x})$ profile of the 220 μm bubbles corresponds to that found in the concentration profile.

Differences between the RMS for bubbles (open symbols) and for fluid *seen* (dashed line) are very small if not negligible also in downflow (Fig. 10). Away from the wall, profiles superpose very closely to the profile of the Eulerian RMS along each flow direction and regardless of the bubble-fluid coupling (with the exception of the streamwise component for the 220 μm bubbles, Fig. 10b and c. Near the wall deviations become large. This may be attributed to bubble preferential segregation in high-speed zones, where the intensity of turbulent fluctuations is higher than the mean. However, the presence of spikes in the RMS profiles suggests that downflow statistics might be affected by the small number of bubbles in the very near-wall region.

Finally, we examine bubble preferential distribution in the low-speed/high-speed regions of the flow, and in Fig. 11 we show the Probability Density Function (PDF) of the streamwise fluid velocity fluctuation, $(u'_x)_{@p}$, evaluated at the location of bubbles in the wall region ($5 < z^+ < 15$). To obtain the PDF (i) we subdivided this region into 10 equally-spaced wall-parallel slabs and we calculated the space-averaged streamwise fluid velocity, $\bar{u}_s$, in each slab s; (ii) we determined the slab containing the bubble; (iii) we computed $(u'_x)_{@p} = (u_x)_{@p} - \bar{u}_s$; (iv) we counted the number of bubbles associated with each value of $(u'_x)_{@p}$ and we normalized this number by the total number of bubbles located in the slab. In Fig. 11 an effect of bubble size is apparent. In upflow larger bubbles distribute preferentially in the regions of lower-than-mean fluid velocity whereas smaller bubbles appear more evenly distributed across the threshold value $(u'_x)_{@p} = 0$. In downflow, the PDF of the smaller bubbles is positively skewed indicating that these bubbles sample regions of higher-than-mean fluid velocity more often. The PDF of the larger bubbles is more symmetric and develops a peak exactly at $(u'_x)_{@p} = 0$, indicating no preferential distribution. These results are in agreement with those of Section 3.3.1.

3.4. Spectral analysis of energy modulation

In Fig. 12 we show the one-dimensional streamwise and spanwise dissipative spectra of the fluid, $D(k)$ with k the non-dimensional wavenumber, computed in the near-wall region ($z^+ = 3.4$) and in the center of the channel ($z^+ = 150$). We plot $D(k) = k^2E(k)$ rather than the energy spectrum $E(k)$ to emphasize the modulation of turbulent energy induced by the bubbles. For ease of discussion, we consider the spectra relative to the 220 μm bubbles and rescaled by the upflow/downflow shear velocities of Table 2. We examine first the streamwise dissipative spectra for the upflow case (Fig. 12a), which show interesting modifications due to combined effect of two-way coupling and lift. It is important to observe that, in the unladen flow case, the spectrum in the central region (open squares) crosses over the spectrum in the wall-region (open circles) at wavenumbers $k \simeq 2 \div 3$. Differences are small (and over amplified) at the low wavenumbers, but there is an obvious indication that (as expected) smaller scales possess much more energy in the central part of the channel. If we now consider the spectra in the bubble-laden case, we first observe that there is relatively little difference between the spectra computed in the center of the channel (open squares versus full squares), but we remark that the spectrum in the vicinity of the wall now has much more energy at the larger scales and crosses over the spectrum in the central part of the channel only at a wavenumber $k \simeq 7 \div 8$. Compared to unladen flow (open symbols), the cross-over between the near-wall profile (circles) and the centerline profile (squares) shifts

toward larger wavenumbers. Another relevant feature, which is peculiar of the centerline spectra, is the energy increase (resp. decrease) at dimensionless wavenumbers smaller (resp. larger) than $k_x h = 2$ when two-way coupling is applied (black symbols). A similar behavior has been observed in microbubble-laden homogeneous isotropic flow by van den Berg et al. (2006) and by Mazzitelli et al. (2003a,b), even though at larger scales: In their work, energy modulation is attributed to upward transfer of momentum associated to lift-induced accumulation of bubbles on the downflow side of vortices. Spectra do not cross each other in the near-wall region, indicating that the effect of bubbles mimics an energy source at all scales, especially the smallest. This behavior can be ascribed to a twofold effect of lift: first, lift favors stronger energy input by accumulating bubbles at the wall; second, lift induces an increase of drag (as discussed in Section 3.5) which generates higher momentum transfer and in turn higher energy exchange. This mechanism can explain also why spanwise spectra (shown Fig. 12b) attain higher values in two-way coupled upflow regardless of the distance from the wall at which they are computed. An opposite reasoning applies to the downflow case (Fig. 12c and d), where bubbles back-reacting on the flow can be regarded as a sink of energy: bubbles drain and dissipate energy from the flow, damping turbulence at all scales and along all homogeneous directions (no cross-over). Accordingly, the location at which the near-wall and the centerline streamwise spectra cross each other in Fig. 12c occurs at larger scales. The spectral analysis of energy

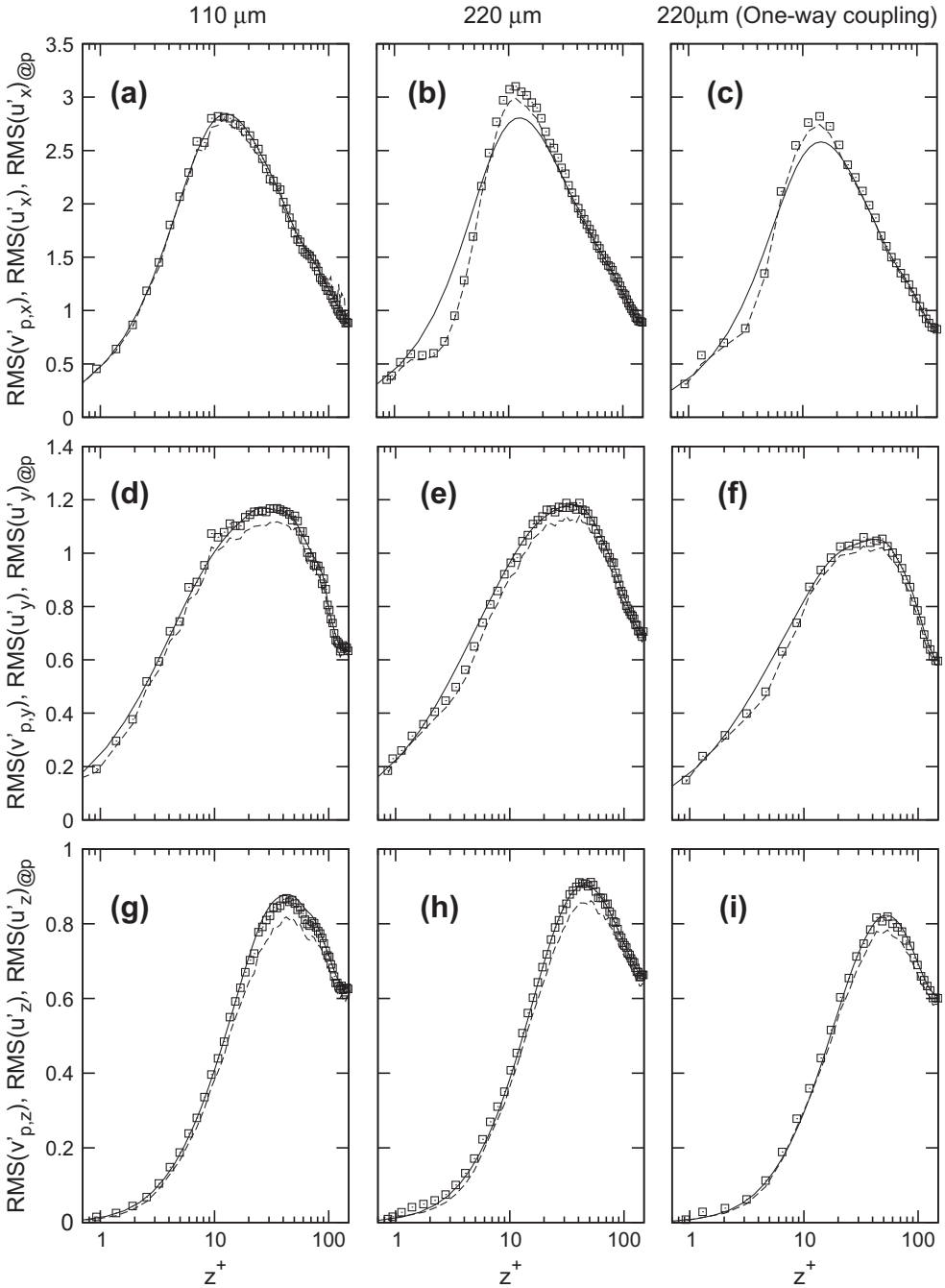

Fig. 9. RMS of bubble velocity, $RMS\left(v'_{p,x}\right)$ (□); of Eulerian fluid velocity, $RMS(u'_x)$ (—); and of fluid velocity at bubble location, $RMS(u'_x)_{@p}$ (- - -) in upflow. Rows–Panels (a–c): streamwise component; panels (d–f): spanwise component; panels (g–i): wall-normal component. Columns–Panels (a), (d), and (g): two-way coupled upflow with 110 μm bubbles; panels (b), (e), and (h): two-way coupled upflow with 220 μm bubbles; panels (c), (f), and (i): one-way coupled upflow with 220 μm bubbles.

modulation in upflow (resp. downflow) is in agreement with the increase (resp. decrease) of all fluid RMS components observed in Fig. 4 (symbols versus thin dashed lines). We remark here that the predicted levels of energy enhancement or attenuation are influenced not only by the two-way coupling model, but also by the model of the lift force (Eqs. (4) and (9)) and in particular by the value of the lift coefficient adopted in the calculations: inaccuracies in the choice of this coefficient will produce wrong energy input, leading to erroneous and even qualitatively different results (van den Berg et al., 2006). Clearly, this rises issues concerning the specific lift force model used.

3.5. Is it the correct lift force model?

Lift force models have been proven adequate in homogeneous isotropic turbulence (Mazzitelli et al., 2003a,b), where lift is determined uniquely by local velocity gradients. However, their applicability to non-homogeneous anisotropic shear flows, where local gradients co-exist with shear-induced mean gradients, is still debatable. This issue is crucial in the high-shear regions (e.g. near the wall in channel or pipe flow), where lift is mostly determined by mean velocity gradients. In these regions, prediction of bubble dynamics will be largely affected by minimal variations of the model coefficients.

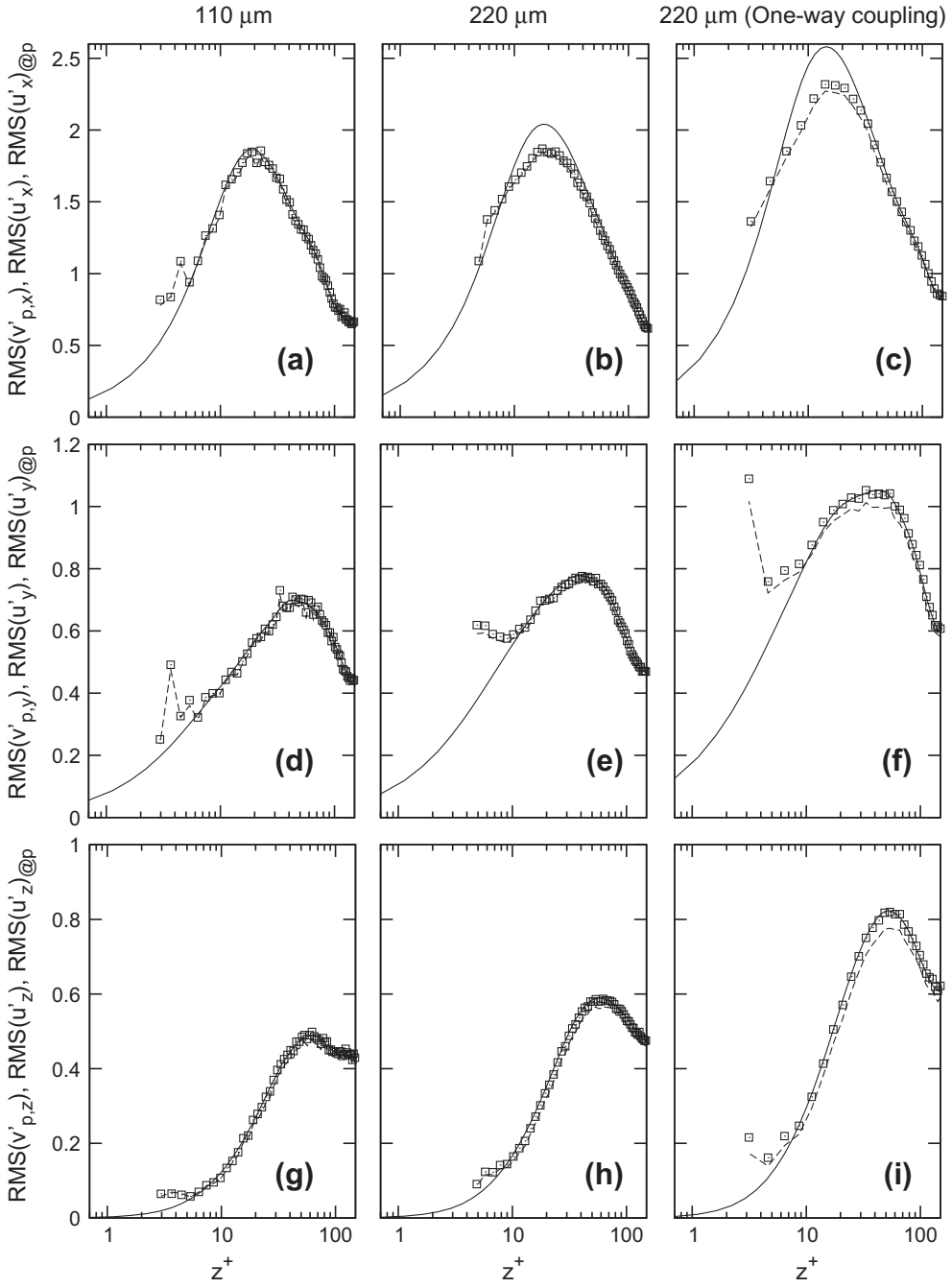

Fig. 10. RMS of bubble velocity, $RMS\left(v'_{p,x}\right)$ (□); of Eulerian fluid velocity, $RMS(u'_x)$ (—); and of fluid velocity at bubble location, $RMS(u'_x)_{@p}$ (- - -) in downflow. Rows–Panels (a–c): streamwise component; panels (d–f): spanwise component; panels (g–i): wall-normal component. Columns–Panels (a), (d), and (g): two-way coupled downflow with 110 μm bubbles; panels (b), (e), and (h): two-way coupled downflow with 220 μm bubbles; panels (c), (f), and (i): one-way coupled downflow with 220 μm bubbles.

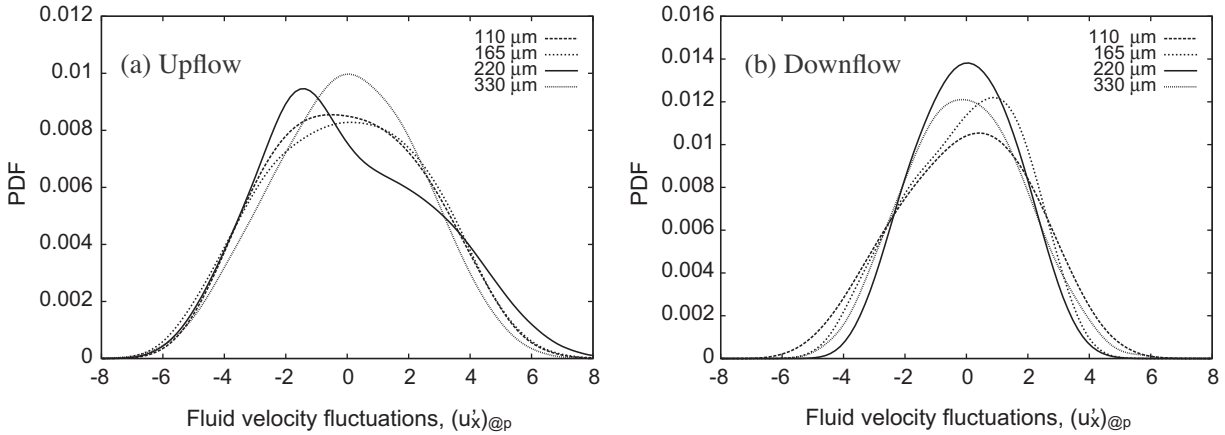

Fig. 11. Probability distribution function (PDF) of streamwise fluid velocity fluctuations, $(u_x')_{@p}$. Panels: a) upflow; b) downflow. Lines: (– – –) 110 μm bubbles; (- - - -) 165 μm bubbles; (—) 220 μm bubbles; (· · · · · ·) 330 μm bubbles.

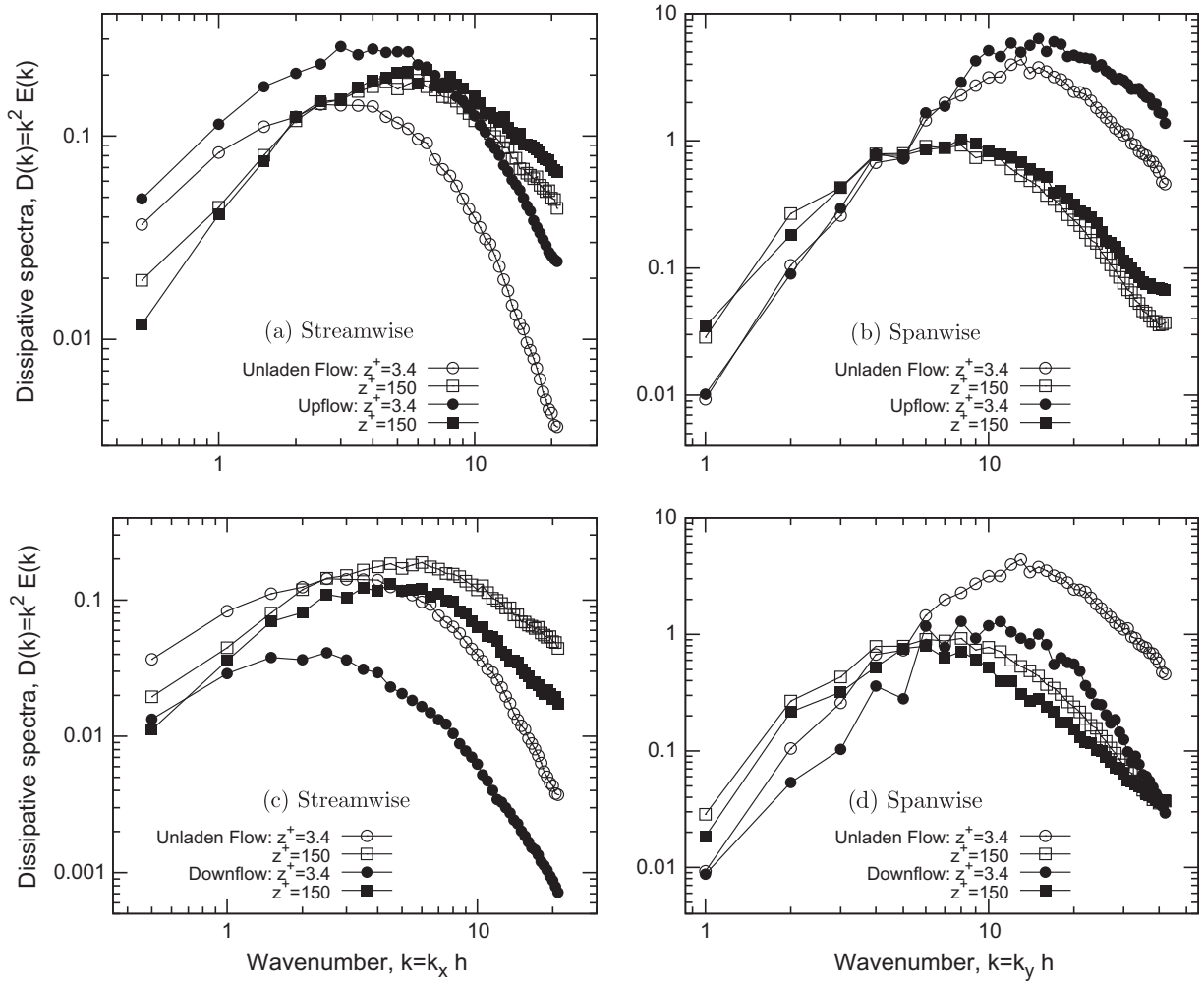

Fig. 12. One-dimensional dissipative spectra of the fluid, $D(k) = k^2 E(k)$, computed at two different wall-normal locations: $z^+ \simeq 3.4$ in the near-wall region (circles: ○, ●), and $z^+ \simeq 150$ in the center of the channel (boxes: □, ■). Open symbols refer to unladen flow simulations, black symbols refer to two-way coupling simulations with the 220 μm bubbles. Panels: (a and b) upflow; (c and d) downflow; (a and c) streamwise spectra; (b and d) spanwise spectra.

In Figs. 13 and 14 we look at the relative importance of the forces acting on bubbles. In Fig. 13 the wall-normal components of these forces are shown for the upflow case. Streamwise components are not shown here as they just show perfect balance between buoyancy and drag, as discussed in Giusti et al. (2005); spanwise components will not be discussed either, as they are rather irrelevant to bubble macroscopic behavior in the present flow configurations. From Fig. 13a, which shows only results for

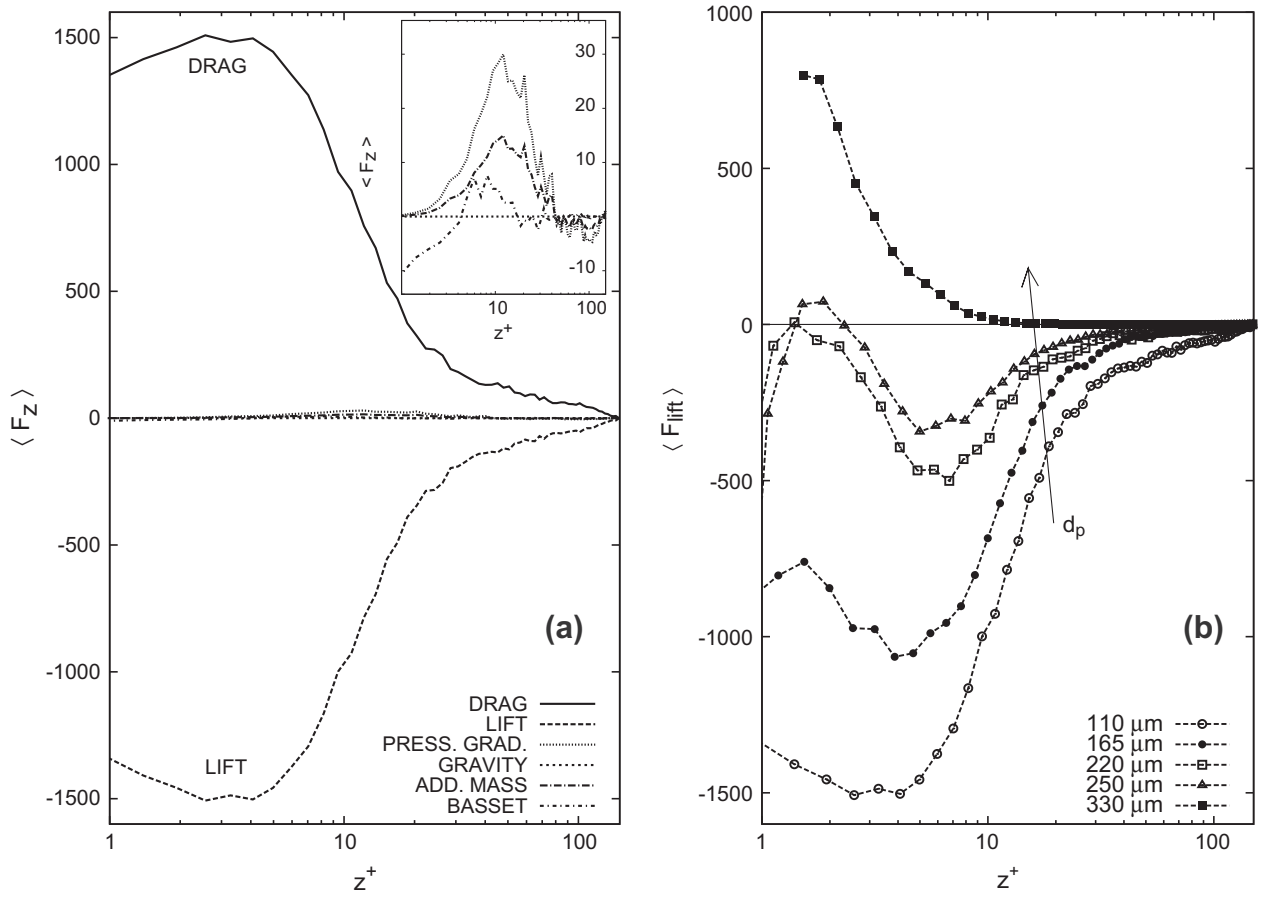

Fig. 13. Wall-normal component of the forces acting on bubbles in upflow. Panel (a), relative to the 110 µm bubbles only, shows that drag and lift are the dominant forces and counterbalance each other. Panel (b) shows the behavior of lift force only for all bubble classes.

the 110 µm bubbles to simplify discussion, it is apparent that there is no dominant effect as long as bubbles sample the center of the channel while drag and lift dominate in the near-wall region with peak values of order $\mathcal{O}(10^3)$. Compared to drag and lift, all other forces are negligible in the region $0 < z^+ < 40$ where their peak values are of order $\mathcal{O}(10)$ as shown by the inset in each panel of Fig. 13a. This behavior is common to all bubble classes, therefore only the lift profiles are plotted in Fig. 13b, which we examine to analyze force behavior at varying bubble size. In this figure, we also include the result relative to the 250 µm bubbles as it adds to the discussion. The following observations can be made. First, the order of magnitude of lift (and hence drag) in the present two-way coupling simulations is lower than that obtained in one-way coupling simulations (Giusti et al., 2005) and agreement with experimental data (see Ogasawara et al., 2004 for instance) is improved. This can be ascribed to the inclusion of wall effects in the lift force model, which appears to allow a more realistic representation of the physics. Second, there is a significant change of shape and even of sign among the different profiles. For the smallest bubbles (d_p = 110 µm) the lift force is always negative (i.e. directed toward the wall) and exhibits one minimum at $z^+ \simeq 3$. As bubble size increases, the lift force becomes less negative until reversal of the force occurs and profiles develop a local maximum very near the wall: this maximum is still negative for the 165 µnm bubbles, is equal to zero for the 220 µm bubbles and becomes positive for the 250 µm bubbles. For the largest bubbles (d_p = 330 µm), the lift force is always positive (i.e. directed away from the wall) and values increase monotonically as the wall is approached. Forces in downflow are shown in Fig. 14. Results in Fig. 14a lead to the same observations drawn from Fig. 13a. As expected, values for lift are smaller than in one-way coupling simulations, always positive and increasing near the wall. Fig. 14b, however, shows that the magnitude of the lift force increases for decreasing bubble size. The rather surprising trends shown in Figs. 13 and 14b are due to the extra lift force induced by the presence of the wall. Thus we must expect significant sensitivity of numerical predictions to the model coefficients (C_{LW} in this case) when evaluating such figures.

To complete the analysis, in Fig. 15 we show the wall-normal behavior of the two contributions to the total lift force (which is indicated as F_{lift} in this figure): $f_L = C_L \frac{\rho}{\rho_p}\left\{[(u_z)_{@p} - v_{p,z}] \times \boldsymbol{\omega}\right\}$ and f_{LW} as defined in Eq. (9). Profiles were computed at the end of the simulations and refer to the 220 µm bubbles, chosen here as reference for the discussion (results for the other bubble sets are qualitatively similar and will not be shown). From Fig. 15 it is apparent that wall-induced effects on lift are noticeable only for $z^+ \leqslant 10$. In addition, the relative contribution of f_L and f_{LW} become comparable well inside the viscous sublayer-few viscous units from the wall-in upflow (Fig. 15a), whereas f_L appears to be always significantly larger than f_{LW} in downflow (Fig. 15b).

4. Conclusions

In this paper we have presented results from direct numerical simulations of turbulent microbubble dispersion in vertical channel flow for both upflow and downflow conditions. Bubbles interact with the surrounding fluid by exchanging momentum. The main macroscopic effect produced by bubble collective behavior

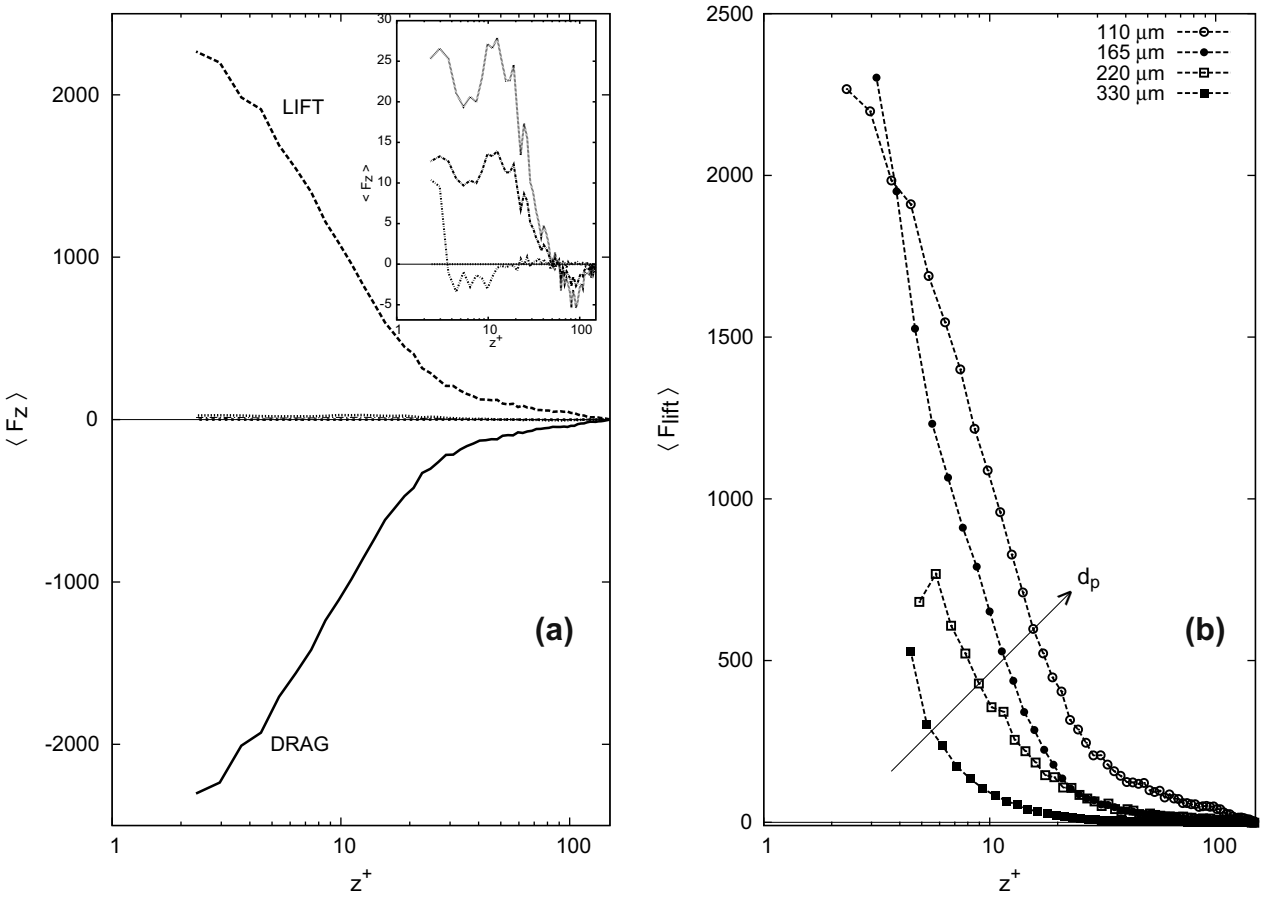

Fig. 14. Wall-normal component of the forces acting on bubbles in downflow. Panel (a), relative to the 110 μm bubbles only, shows that drag and lift are the dominant forces and counterbalance each other. This behavior is common to all bubble classes. Panel (b) thus focuses on the behavior of the lift force only for all bubble classes.

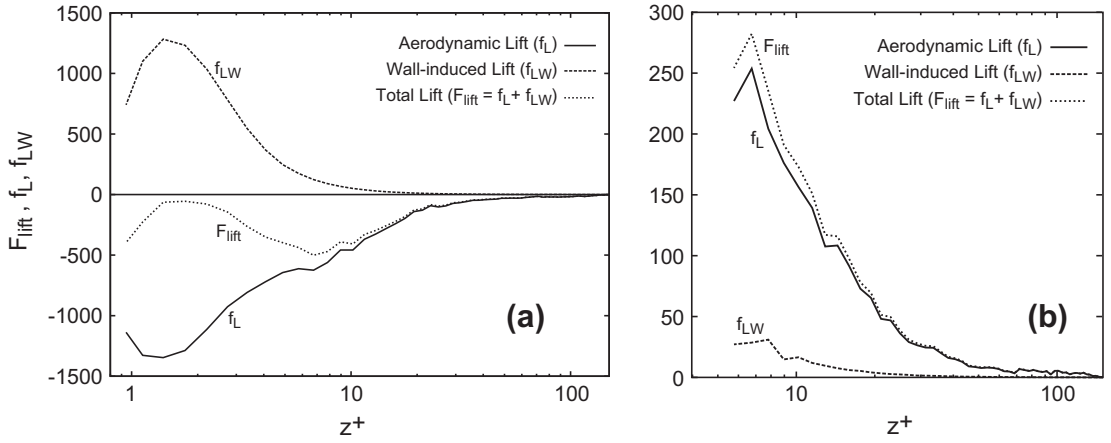

Fig. 15. Instantaneous wall-normal component of the total lift force, F_{lift}, and of its contributions, f_L and f_{LW}, for the 220 μm bubbles. Panels: (a) upflow, (b) downflow.

is an increase (resp. decrease) of the liquid flowrate in upflow (resp. downflow) associated with modifications of the shear stress at the wall. We have proposed a simple one-dimensional model to rescale the wall shear stress based on the overall force balance on the channel, including explicitely the force exerted by the bubbles on the fluid. This rescaling is applied to examine two-phase flow statistics and is useful to explain turbulence modifications associated to wall shear stress modifications.

As in previous one-way coupling simulations of the same flow domain (Giusti et al., 2005), we observe strong wallward migration and wall accumulation in upflow, favored by lift effects on the interaction between bubbles and near-wall turbulent structures. No accumulation build-up is observed in downflow. Analysis of the near-wall bubble distribution shows preferential segregation in low-speed (resp. high-speed) regions, for the upflow (resp. downflow) case.

To evaluate bubble-induced flow field modifications, we have compared two-phase and single-phase dissipation spectra. In upflow, we find enhancement (resp. attenuation) of energy at small (resp. large) flow scales in the channel centerline, whereas energy is always increased by bubbles near the wall. In downflow, no energy cross-over from large to small scales is observed and bubbles always drain energy from the fluid. These findings are directly associated with the specific model of the lift force and with the value of the lift force coefficient, which is known to affect the energy input from bubbles (Mazzitelli et al., 2003a,b). We have tried to underline the impact of the lift force model on present results by examining its wall-normal behavior. Regardless of the flow configuration, in the near-wall region lift dominates over all other unsteady forces acting on the bubbles and is counter-balanced only by drag. Because of the extra contribution due to wall effects (Takemura and Magnaudet, 2003), lift changes sign (from negative, i.e. directed to the wall, to positive, i.e. directed away from the wall) in upflow when bubbles with diameter larger than 220 μm are considered. For these bubbles, reversal of the lift force leads to uniform wall-normal distribution and negligible preferential concentration. Wall effects are also responsible for the lift force reduction that is obtained in downflow when bubble size is increased.

Acknowledgments

Financial support from Italian Ministry for University and Research in the frame of PRIN program under Grant 2003099224_002 is gratefully acknowledged. The authors would also like to thank CINECA for the computational resources (Iscra Grant HP10CXIYES) that were used in this study.

References

Calzavarini, E., van den Berg, T.H., Toschi, F., Lohse, D., 2008. Quantifying microbubble clustering in turbulent flow from single-point measurements. Phys. Fluids 20, 0040702.
Climent, E., Magnaudet, J., 1999. Large-scale simulations of bubble-induced convection in a liquid layer. Phys. Rev. Lett. 82, 4827–4830.
Climent, E., Magnaudet, J., 2006. Dynamics of a plane upflowing bubbly mixing layer: bubble dispersion and effect of two-way coupling. Phys. Fluids 18, 103304.
Crowe, C.T., Stock, D.E., Sharma, M.P., 1977. The Particle-Source-In Cell (PSI-CELL) model for gas-droplet flows. J. Fluids Eng. 99, 325–332.
Delnoij, E., Kuipers, J.A.M., van Swaaij, W.P.M., 1999. A three-dimensional CFD model for gas-liquid bubble columns. Chem. Eng. Sci. 54, 2217–2226.
Elghobashi, S.E., 1994. On predicting particle-laden turbulent flows. Appl. Sci. Res. 52, 309–329.
Elghobashi, S.E., Truesdell, G.C., 1992. Direct simulation of particle dispersion in a decaying isotropic turbulence. J. Fluid Mech. 242, 655–700.
Ervin, E.A., Tryggvason, G., 1997. The rise of bubbles in a vertical shear flow. J. Fluid Eng. 119, 443–449.
Esmaeeli, A., Tryggvason, G., 2005. A direct numerical simulation study of the buoyant rise of bubbles at $O(100)$ Reynolds number. Phys. Fluids 17, 093303.
Felton, K., Loth, E., 2001. Spherical bubble motion in a turbulent boundary layer. Phys. Fluids 13, 2564–2577.
Felton, K., Loth, E., 2002. Diffusion of spherical bubbles in a turbulent boundary layer. Int. J. Multiphase Flow 28, 69–92.
Ferrante, A., Elghobashi, S.E., 2003. On the physical mechanisms of two-way coupling in particle-laden isotropic turbulence. Phys. Fluids 15, 315–329.
Ferrante, A., Elghobashi, S.E., 2004. On the physical mechanisms of drag reduction in a spatially-developing turbulent boundary layer laden with microbubbles. J. Fluid Mech. 503, 345–355.
Fukagata, K., Zahrai, S., Kondo, S., Bark, F.H., 2001. Anomalous velocity fluctuations in particulate turbulent channel flow. Int. J. Multiphase Flow 27, 701–719.
Gatignol, R., 1983. The Faxén formulae for a rigid particle in an unsteady non-uniform Stokes flow. J. Med. Appl. 1, 143–160.
Giusti, A., Lucci, F., Soldati, A., 2005. Influence of the lift force in direct numerical simulation of upward/downward turbulent channel flow laden with surfactant contaminated microbubbles. Chem. Eng. Sci. 60, 6176–6187.
Guet, S., Oooms, G., 2006. Fluid mechanical aspects of the gas-lift technique. Ann. Rev. Fluid Mech. 38, 225–249.
Hibiki, T., Goda, H., Kim, S., Ishii, M., Uhle, J., 2004. Structure of vertical downward bubbly flow. Int. J. Heat Transfer 47, 1847–1862.
Hosokawa, S., Tomiyama, A., 2010. Multi-fluid simulation of turbulent bubbly pipe flows. Chem. Eng. Sci. 64, 5308–5318.
Hosokawa, S., Suzuki, T., Tomiyama, A., 2010. Effects of bubbles on turbulence properties in a duct flow. Mult. Sci. Techn. 22, 211–232.
Jacob, B., Olivieri, A., Miozzi, M., Campana, E.F., Piva, R., 2010. Drag reduction by microbubbles in a turbulent boundary layer. Phys. Fluids 22, 115104.
Korpijarvi, J., Oinas, P., Reunanen, J., 1999. Hydrodynamics and mass transfer in an airlift reactor. Chem. Eng. Sci. 54, 2255–2262.
Kurose, R., Komori, S., 1999. Drag and lift forces on a rotating sphere in a linear shear flow. J. Fluid Mech. 384, 183–206.
Lain, S., Broder, D., Sommerfeld, M., 1999. Experimental and numerical studies of the hydrodynamics in a bubble column. Chem. Eng. Sci. 54, 4913–4920.
Lance, M., Bataille, J., 1991. Turbulence in the liquid phase of a uniform bubbly air–water flows. J. Fluid Mech. 222, 95–118.
Lu, J., Tryggvason, G., 2006. Numerical study of turbulent bubbly downflows in a vertical channel. Phys. Fluids 18, 103302.
Lu, J., Tryggvason, G., 2007. Effect of bubble size in turbulent bubbly downflow in a vertical channel. Chem. Eng. Sci. 62, 3008–3018.
Lu, J., Tryggvason, G., 2008. Effect of bubble deformability in turbulent bubbly upflow in a vertical channel. Phys. Fluids 20, 040701.
Lucas, D., Prasser, H.M., Manera, A., 2005. Influence of the lift force on the stability of a bubble column. Chem. Eng. Sci. 60, 3609–3619.
Marchioli, C., Picciotto, M., Soldati, A., 2006. Particle dispersion and wall-dependent turbulent flow scales: implications for local equilibrium models. J. Turbul. 7, 1–12.
Maxey, M.R., Riley, J.J., 1983. Equation of motion for a small rigid sphere in a nonuniform flow. Phys. Fluids 26, 883–889.
Mazzitelli, I.M., Lohse, D., 2009. Evolution of energy in flow driven by rising bubbles. Phys. Rev. E 79, 1539–3755.
Mazzitelli, I.M., Lohse, D., Toschi, F., 2003a. On the relevance of the lift force in bubbly turbulence. J. Fluid Mech. 488, 283–313.
Mazzitelli, I.M., Lohse, D., Toschi, F., 2003b. The effect of microbubbles on developed turbulence. Phys. Fluids 15, L5–L8.
McLaughlin, J.B., 1991. Inertial migration of a small sphere in linear shear flows. J. Fluid Mech. 224, 261–274.
Mudde, R.F., 2005. Gravity-driven bubbly flows. Ann. Rev. Fluid Mech. 37, 393–423.
Mudde, R.F., Harteveld, W.K., van den Akker, H.E.A., 2009. Uniform flow in bubble columns. Ind. Eng. Chem. Res. 48, 148–158.
Ogasawara, T., Tagawa, Y., Fujiwara, A., Takagi, S., Matsumoto, Y., 2004. The clustering phenomena near the wall in a turbulent bubbly channel flow. In: 3rd Int. Symp. on Two-Phase Flow Modelling and Experiments, Pisa, 22–24 September.
Rizk, M.A., Elghobashi, S.E., 1985. The motion of a spherical particle suspended in a turbulent flow near a plane wall. Phys. Fluids 28, 806–817.
Schiller, V.L., Naumann, A., 1933. Über die grundlegenden Berechnungen bei der Schwerkraftaufbereitung. Z. Vereines Ingenieure 77, 318–320.
Serizawa, A., Kataoka, I., Michiyoshi, I., 1975. Turbulence structure of air–water bubbly flow – III: Transport properties. Int. J. Multiphase Flow 2, 247–259.
Serizawa, A., Inui, T., Gotoh, Y., Tanaka, H., Itsumi, M., 2004. Pseudo-laminar characteristic of bubbly flow with micro bubbles and practical applications of micro bubble. In: 42nd European Two-Phase Flow Group Meeting, Genova, June 21–23.
Soldati, A., Banerjee, S., 1998. Turbulence modification by large scale organized electrohydrodynamic flows. Phys. Fluids 10, 1742–1756.
Soldati, A., Marchioli, C., 2009. Physics and modelling of turbulent particle deposition and entrainment: review of a systematic study. Int. J. Multiphase Flow 35, 827–839.
Takemura, F., Magnaudet, J., 2003. The transverse force on clean and contaminated bubbles rising near a vertical wall at moderate Reynolds number. J. Fluid Mech. 495, 235–253.
Thorpe, S.A., 1982. On the clouds of bubbles formed by breaking wind waves in deep water, and their role in air–sea gas transfer. Philos. Trans. Roy. Soc. Lond. A304, 155–210.
Tomiyama, A., Tamai, H., Zun, I., Hosokawa, S., 2002. Transverse migration of single bubbles in simple shear flows. Chem. Eng. Sci. 57, 1849–1858.
Turney, D.E., Banerjee, S., 2008. Transport phenomena at interfaces between turbulent fluids. AICHE J. 54, 344–349.
van den Berg, T.H., Luther, S., Lohse, D., 2006. Energy spectra in microbubbly turbulence. Phys. Fluids 18, 038103.
Xu, J., Maxey, M.R., Karniadakis, G.E., 2002. Numerical simulation of turbulent drag reduction using micro-bubbles. J. Fluid Mech. 468, 271–281.
Yeo, K., Dong, S., Maxey, M.R., Climent, E., 2010. Modulation of homogeneous turbulence seeded with finite size bubbles or particles. Int. J. Multiphase Flow 36, 221–233.
Yuu, S., Ueno, T., Umekage, T., 2002. Numerical simulation of the high Reynolds number slit nozzle gas-particle jet using subgrid-scale coupling large eddy simulation. Chem. Eng. Sci. 56, 4293–4307.